

DTIC FILE COPY

AD-A215 819



DTIC
ELECTE
DEC 27 1989
S B D

SPECTROMETER

THESIS

Robert D. Kaiser
Captain, USAF

AFIT/GEP/ENP/89D-6

DEPARTMENT OF THE AIR FORCE

AIR UNIVERSITY

AIR FORCE INSTITUTE OF TECHNOLOGY

Wright-Patterson Air Force Base, Ohio

DISTRIBUTION STATEMENT A

Approved for public release;
Distribution Unlimited

89 12 26 160

AFIT/GEP/ENP/89D-6

ANALYSIS AND TEST OF A WIDE ANGLE
SPECTROMETER

THESIS

Presented to the Faculty of the School of Engineering
of the Air Force Institute of Technology
Air University
In Partial Fulfillment of the
Requirements for the Degree of
Master of Science in Engineering Physics

Robert D. Kaiser, B.S.
Captain USAF

December 1989

Approved for public release; distribution unlimited

Preface

This thesis describes an analysis and test of a design for a laser warning receiver which provides aircrew warning and collects threat data. The analysis and test includes the optics and detector of the system. It does not include the electronics or software to drive the detector. The purpose of the thesis is to provide enough information to make a go/no-go decision on contracting for a flyable model.

The results were promising. The angle of arrival and wavelength accuracy was adequate. Measurement of the incident pulse energy per unit area showed anomalies which limited its accuracy. The system could detect a laser pulse that is a small fraction of the Maximum Permissible Exposure.

There are several individuals I wish to thank. I'd like to thank my faculty advisor, Capt J. Targove for his advice and support. I am deeply indebted to Mr B. Knight of the Building 450 Fabrication Shop, without whom I never would have finished in time. I am especially indebted to my wife, BJ, who typed and proofread this entire manuscript.

Robert D. Kaiser, Jr.

Accession For	
NTIS GRA&I	<input checked="" type="checkbox"/>
DTIC TAB	<input type="checkbox"/>
Unannounced	<input type="checkbox"/>
Justification	
By	
Distribution/	
Availability Codes	
Dist	Avail and/or Special
A-1	

Table of Contents

	Page
Preface	ii
List of Figures	v
List of Tables	vii
Abstract	viii
I. Introduction	1
Principle of Operation	3
II. Design	6
Detector	6
Spectrometer	8
Fisheye Lens	10
Copy Lens	12
Cylindrical Lens	14
Field Lens	19
Fiber bundle	21
Neutral Density Filters	24
Extending the Useable Range Through 1.06 microns	26
Measuring Pulse Energy	28
Maximum Pulse Repetition Frequency Discernible.	29
Modeling	29
III. Implementation and Component Tests	31
The Test Bench	31
Detector	36
CCD Array	36
CID Array	38
Spectrometer	39
Fisheye Lens	45
Field Lens	48
F-Number Matching	50
Alignment	52
IV. System Test	59
Spot Size	59
Wavelength Calibration and Testing	63
Angle of Arrival Calibration and Testing	67
Pulse Energy Calibration and Testing	69

Minimum Laser Pulse Energy Detectable . .	74
Saturation Behavior	76
V. Conclusions	78
Bibliography	81
vita	82

List of Figures

Figure	Page
1.1. Simplified system diagram	4
2.1. Cylindrical lens orientation.	15
2.2. Determination of f_{cy}	16
2.3. Notation used in f_{cy} vs d calculation.	17
2.4. Effect of the field lens.	20
2.5. Effect of off-axis objects on fiber f/#	22
3.1. Test bench layout	32
3.2. Pulse Energy vs prf (Nd:YLF).	35
3.3. CCD detector response	38
3.4. CP-200 spectrometer	39
3.5. Notation used in derivations involving the CP-200 spectrometer	42
3.6 Dispersion vs column number	44
3.7. Bandpass vs column number	45
3.8. Fisheye lens.	46
3.9. H vs AOA for the fisheye lens	47
3.10. Displacement of entrance pupil vs AOA	48
3.11. Power transmitted vs AOA for entrance optics.	50
3.12. FWHM vs defocus of fiber bundle face.	58
4.1. Spectrum width vs AOA for the arc lamp.	60
4.2. Spot size vs AOA for the Nd:YLF	61
4.3. X and Y cross-sections of a laser spot.	62
4.4 Wavelength vs column number for the CCD array	66

4.5.	Row number vs AOA	68
4.6.	System responsivity vs AOA, wide field.	70
4.7.	System responsivity vs wavelength	71
4.8.	System responsivity vs AOA, narrow field.	73
4.9.	Saturation Behavior	77

List of Tables

Table	Page
3.1. Legend for test bench layout.	33
3.2 Data from NA_{out} measurement of fiber bundle . . .	51
4.1 Wavelength calibration data	66

Abstract

A design for a device to measure wavelength, angle of arrival, and energy of a laser pulse is analyzed and tested. The instrument has a 180° field of view and an operating range of 400 nm - 800 nm. In a series of tests the instrument was found to measure angle of arrival accurately to within ± 41 arc minutes and a wavelength to within 1 nm. A variation of $\pm 20\%$ in the measurement of pulse energy per unit area was found for small changes in angle of arrival. The system was thermal noise limited and could detect a pulse that was $1/45$ of the Maximum Permissible Exposure (MPE) with an uncooled detector. When using a detector cooled to -10°C , the system could detect a pulse $1/22000$ of the MPE.

ANALYSIS AND TEST OF A WIDE ANGLE SPECTROMETER

I. Introduction

US Air Force aircrews and sensors are vulnerable to blinding or dazing laser radiation from enemy ground sources. Avionics to validate this threat, classify its source, provide aircrew warning and give threat location is needed.

This research is an attempt to design, analyze, prototype, and test an approach to meeting this need which uses a cylindrical lens and a spectrometer equipped with an area detector. The goal of this thesis is to provide the appropriate government agencies with enough information to make a go/no-go decision to contract for a flyable model. Data from this thesis may aid in the writing of a contract specification, should the decision to go ahead be made.

Testing in this thesis is limited to the entrance optics, spectrometer, and detector. The hardware and software required to drive the detector and algorithms to process the data are specifically excluded. The performance of these items is strongly dependent on the hardware

architecture selected and the programming algorithm used, both of which are out of the author's area of expertise.

This thesis consists of five chapters; Introduction, Design, Implementation and Component Test, System Test, and Conclusions. Chapter I states the purpose of the thesis and outlines the basic design approach used. Information here should be of interest to all readers. Chapter II is an analysis of the design. It primarily focuses on design parameter trade-offs and how they affect system performance. The intended audience of this chapter is the optical engineer or system designer interested in improving on the design or adapting it to meet a changing need. Chapter III describes the specific equipment used to conduct the tests. It is included to provide detailed information on the specific hardware used and to define the limits to the applicability of the test results. Chapter IV details the tests conducted and presents the results. It represents the culmination of the work done on this thesis. Chapter V summarizes the test results and provides recommendations for further research.

In order to optimize the design, certain assumptions had to be made about the equipment's purpose and its operating environment. It was assumed that the order of priority for the system performance factors was:

- (1) Accuracy of wavelength measurement

- (2) Accuracy of angle of arrival (AOA) measurement
- (3) Minimum Laser Pulse Energy Detectable (MED)
- (4) Accuracy of pulse energy per unit area measurement
- (5) Dynamic range of the detector (saturation energy/noise equivalent energy)
- (6) Maximum pulse repetition frequency (prf) discernable

It was further assumed that a wavelength range from 400-800 nm, a field of view of 180°, and an availability near 100% was required.

It was assumed that a production system would be mounted on cargo or reconnaissance aircraft and that an extension to fighters was desirable. Hence, light weight, small size, and rugged construction was preferred. It was also assumed that the prototype produced for this thesis would be for lab use only and would not be flown.

Principle of Operation

This section provides a basic overview of the design approach. Considerably more detail on the relationship between components is provided in Chapters II and III, but an understanding of the basic system is conveyed here so one does not get lost in the details. A simplified system diagram is shown in Figure 1.1. The core of the system has five main parts: a fisheye lens, a field lens, a

combination copy lens/cylindrical lens, a coherent fiber bundle, and a spectrometer configured with a charge coupled device (CCD) or charge injection device (CID) detector.

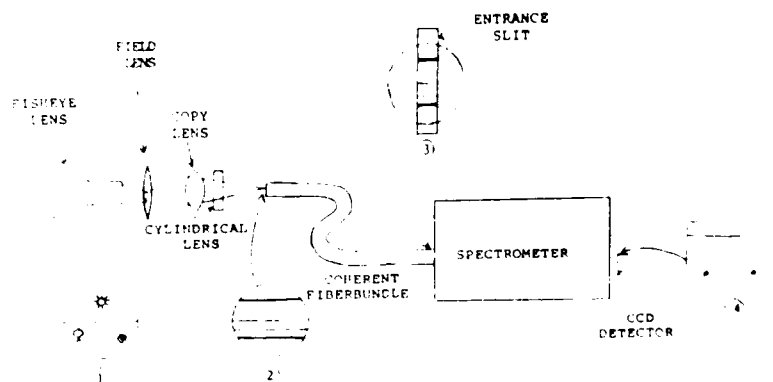


Figure 1.1. Simplified system diagram.

The fisheye lens collects light from a 180° field of view. It produces an intermediate image as shown in plane 1 in Figure 1.1.

The field lens prevents vignetting, which occurs when light from objects near the edge of the field of view miss the copy lens. It does not alter the size or shape of the final image.

The copy lens, which acts like a photographic enlarger lens, when combined with the cylindrical lens serves two purposes. First, the copy lens reimages the light onto the fiber bundle. Second, the cylindrical lens smears the light onto the fiber bundle face horizontally. This effect can be seen in plane 2 of Figure 1.1. This insures that some light

from all objects is incident on the central region of the bundle yet maintains any vertical separation that exists between the objects. Smearing the light with the cylindrical lens is important since only the light incident on the central region of the bundle will pass the entrance slit and enter the spectrometer.

The coherent fiber bundle consists of hundreds of millions of tiny optical fibers which maintain the same relative orientation to one another over the length of the bundle. The fiber bundle is used to transfer the image from the bundle face to the entrance slit of the spectrometer.

The spectrometer is equipped with a two dimensional (2D) CCD array. At the detector, spectra will appear horizontally. However, the spectrum from an object at one height on the entrance slit will be separated vertically from the spectrum of an object at another height, as shown in Figure 1.1. In this manner the spectrum of an incident laser pulse will be separated from the spectrum of the sun and other background objects. It also gives one dimension of AOA of the pulse, since the height of the spectrum can be directly related to AOA. In an operational scenario a second system with its fiber bundle face and cylindrical lens rotated 90° with respect to the first system, would provide the AOA in a plane perpendicular to the first. This would define the AOA uniquely.

II. Design

This chapter describes the trade-offs involved in the design of the system outlined in Chapter I. The effects of design parameters such as cylindrical lens focal length and detector clock rate on the system performance is discussed in detail. As much general information as can be provided without detailing specific instruments is included. Additional information pertaining only to the specific equipment tested is reserved for Chapter III. The sections of this chapter are roughly in the order in which the components were selected. As with all systems, this design was an iterative process.

Detector

The primary design parameters of interest for the detector are: total number of pixels, pixel size, saturation energy and Noise Equivalent Energy (NEE). As the spectrum of an object is focused onto the detector, the number of pixels this spectrum covers determines the minimum accuracy of the wavelength measurement.

To maximize the wavelength resolution, a small pixel width is necessary. The trade off here is that the smaller the pixel, the more of them are required for a given wavelength range. Assuming the clock rate and size of the spectrum is fixed, this results in a slower frame rate and a

corresponding loss in temporal definition (i.e., the slower the frame rate, the lower the pulse repetition frequency (prf) that can be resolved). A slower frame rate also results in decreased signal-to-noise (S/N) and signal-to-background (S/B) ratios if one assumes a pulsed threat laser in a continuous background.

The saturation energy determines the maximum laser energy the detector can accurately measure. The Noise Equivalent Energy (NEE) is the amount of energy per unit area on the detector which provides an output equal in magnitude to the noise. NEE determines the Minimum Laser Pulse Energy Detectable (MED). The saturation energy divided by the NEE is called the dynamic range of the detector. Neutral density filters can be used to raise the maximum pulse energy and MED. They effect the energy incident on the detector, but do not change the dynamic range of the detector. This will be more thoroughly discussed in the section "Neutral Density Filters" in this chapter.

In selecting a detector RS-170 compatibility should be considered. RS-170 compatibility allows the data from the detector to be stored on a standard VHS videocassette recorder. The trade-off is that RS-170 compatibility requires a 30 Hz frame rate and 2:1 interlacing. In 2:1

interlacing every even numbered line on the detector and then every odd numbered line on the detector, is read.

Also of interest is how the detector responds when saturated. CCD arrays are known to "bloom" when saturated in the direction they are read out. In this system blooming results in loss of wavelength information. CID arrays are reported by the manufacturer not to do this. In Chapter IV, a comparison of blooming characteristics between a CCD detector and a CID detector is given.

For this project we selected an EG&G 1430-P CCD detector. It had an array of 576 X 384 square format pixels, with a 23 micron center to center distance. The dynamic range was 5200 when operated at -10°C. We also selected a CIDTEC model 2250A4 CID array. It had an array of 512 X 512 square format pixels with a 15 micron center to center distance. The dynamic range was 200. The model 1430-P CCD detector was selected because there was an OMA system available in house to drive it. The model 2250 CID detector was selected for similar reasons.

Spectrometer

The primary design parameters of interest for the spectrometer are astigmatism correction, focal length, grating groove density, and entrance slit height. Most spectrometers are prone to astigmatism. Astigmatism in a

spectrometer causes a point source in the entrance slit to be imaged as a vertical line in the focal plane. This causes a loss of AOA information. The astigmatism as well as other aberrations can be corrected by the use of a holographic grating rather than a standard ruled grating.

The focal length and grating groove density together determine the dispersion of the spectrometer. The dispersion to a first-order approximation is given by Equation 2.1. (2:5)

$$\frac{dl}{dx} := \frac{1}{g \cdot m \cdot f} \quad (2.1)$$

Here, dl/dx is the dispersion in nm/mm, g is the groove density, m is spectral order, and f is the focal length of the instrument.

By dividing the wavelength range of interest by dl/dx one approximates the width of the spectrum in the focal plane. This must be matched to the detector width, so the selection of a spectrometer and a detector is best done simultaneously.

The entrance slit height should be matched to the detector height. If the slit is too small then only a portion of the detector is used. If it is too large then information is lost at the top and bottom of the detector.

Slit width is another design parameter. A narrow slit allows more wavelength resolution. However, a narrow slit lets less light through and therefore raises the MED. This is more thoroughly discussed in the section "Neutral Density Filters," in this chapter.

We selected an Instruments S.A. CP-200 spectrometer. It had a 133 grooves/mm corrected holographic grating and a 200 mm focal length. The CP-200 was selected because of its small size, rugged construction, ability to accept a 2D array and because it would cover the 400 nm range required on both detectors. The entrance slit height of 6 mm made only 260 of the 384 rows on the CCD detector useful.

Fisheye Lens

The primary design factors of the fisheye lens are its focal length, field of view, and f-number (f/#). Fisheye lenses, unlike other lenses, have a linear relation between angle of arrival (AOA) and location of the image in the focal plane (Equation 2.2). (1:1061)

$$H = \text{AOA} \times f \quad (2.2)$$

Here, H is the distance from center of the focal plane, f is the focal length of the fisheye, and AOA is in radians.

This relationship allows for a linear correspondence between row number on the detector (y), to AOA. It also shows the importance of the focal length of the lens since $\pi * f$ will be the diameter of the intermediate image. In general, the size and weight of a fisheye is inversely proportional to its focal length and directly proportional to its field of view. That is to say, fisheyes with large field of views and short focal lengths tend to be larger and heavier.

The $f/\#$ of the lens determines how much light enters the system. In most cases the $f/\#$ is not a concern since neutral density filters are required to keep a laser pulse on the order of the Maximum Permissible Exposure (MPE) from saturating the detector.

One item to be aware of when selecting a fisheye lens is vignetting. If vignetting increases greatly with AOA, then an object on the edge of the field of view will appear dimmer than one in the middle. This would contribute to the AOA dependence in the measurement of pulse energy¹ and raise the MED for objects toward the edge of the field of view.

We selected a Nikkor 8 mm $f/2.8$ fisheye. This lens was selected because it had a 180° field of view and was a stock item.

¹For the purposes of this thesis the term "pulse energy" will be used to mean the energy per unit area incident upon the fisheye lens by a pulsed laser source.

Copy Lens

The purpose of the copy lens is to reimage the light from the fisheye onto the face of the fiber bundle, reducing or magnifying it to the size of the entrance slit in the process. In selecting a copy lens, both focal length and $f/\#$ are important.

The focal length will determine the overall length of the entrance optics. Using both the gaussian lens formula and the definition of magnification (Equations 2.3 and 2.4) for a given focal length one can find s_o and s_i (Equations 2.5 and 2.6).

$$\frac{1}{f_{co}} := \frac{1}{s_o} + \frac{1}{s_i} \quad (2.3)$$

$$|M| := \frac{s_i}{s_o} \quad (2.4)$$

$$s_i := f_{co} \cdot (1 + |M|) \quad (2.5)$$

$$s_o := \frac{s_i}{|M|} \quad (2.6)$$

In these equations, f_{co} is the effective focal length of the copy lens, M is the magnification, s_o is the distance from the back focal plane of the fisheye to the copy lens, and s_i is the distance from the copy lens to the face of the fiber bundle. The overall length can be found using Equation 2.8.

$$OAL := BFL_{fe} + s_o + s_i \quad (2.7)$$

$$OAL := BFL_{fe} + f_{co} \left[2 + |M| + \frac{1}{|M|} \right] \quad (2.8)$$

A multi-element copy lens will minimize the aberrations in the entrance optics. The aberrations determine the spot size which, in this design, is a limiting factor in AOA accuracy. The above equations, which were derived assuming thin lenses, still hold if s_o is measured to the copy lens first principal plane, s_i is measured from the copy lens second principal plane, and the distance between the principal planes is included in the overall length.

The copy lens will, in general, be the aperture stop for the system. Therefore, the $f/\#$ of the copy lens directly affects the MED. Since for most lenses, aberrations go up as the $f/\#$ goes down, selecting the $f/\#$ becomes a trade-off between system throughput and spot size. Only through a detailed lens model can the actual tradeoff be quantified.

We selected a COMPONON-S 50 mm f/1.3 TV camera lens. The 50 mm was the shortest focal length lens we could find with an entrance pupil diameter of at least 35 mm. It resulted in a overall length of approximately 330 mm.

Cylindrical Lens

The three design parameters for the cylindrical lens are its focal length, size, and position. The purpose of the cylindrical lens is to make the cylindrical/copy lens combination have two different focal lengths: one in the plane parallel to and one in the plane perpendicular to the long axis of the entrance slit, i.e. the tangential and sagittal planes respectively. This is illustrated in Figure 2.1.

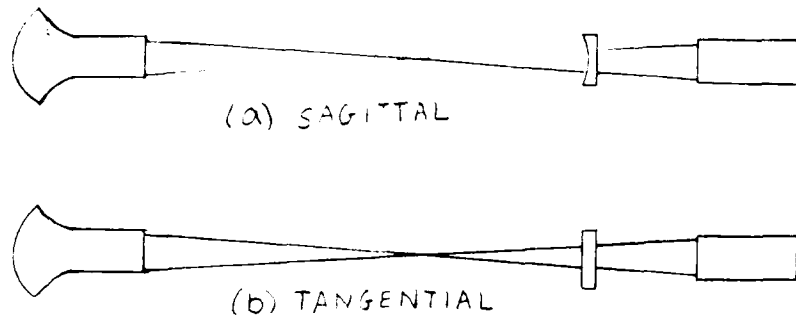


Figure 2.1. Cylindrical lens orientation.
(a) The sagittal plane is perpendicular to the entrance slit. (b) The tangential plane includes the entrance slit.

Through an appropriate choice of focal length and position of the cylindrical lens, the length of the line of light on the fiber bundle face, i.e. the focal line, is made longer than the diameter of the image. This is shown in Figure 2.2. This guarantees that some light from every object in the field of view will get through the entrance slit.

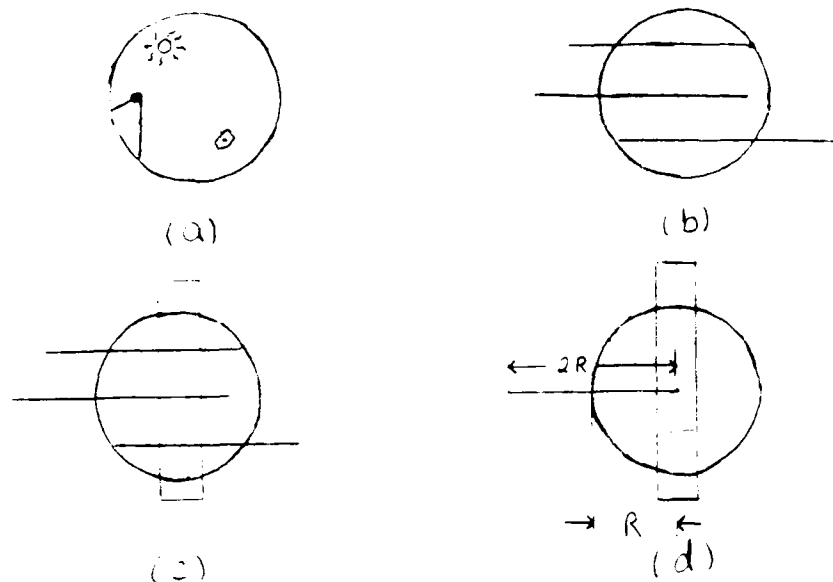


Figure 2.2. Determination of f_{cy} . (a) The image at the fiber bundle without the cylindrical lens. (b) Image at the fiber bundle with the cylindrical lens. (c) Image with the entrance slit superimposed. (d) Worst case. Focal line must be at least twice the radius of the image at the fiber bundle face.

One can use the gaussian lens formula to find the sagittal and tangential focal lengths of the two lens combination, as given in Equations 2.9 and 2.10.

$$f_t := f_{co} \quad (2.9)$$

$$\frac{1}{f_s} := \frac{1}{f_{co}} + \frac{1}{f_{cy}} - \frac{d}{f_{co} \cdot f_{cy}} \quad (2.10)$$

Here, f_{co} is the effective focal length of the copy lens, f_{cy} is the effective focal length of the cylindrical lens, f_s is the sagittal focal length of the two lens combination, f_t is the tangential focal length of the two lens combination, and d is the distance between the two lenses, as measured from the principal planes.

For a given copy lens and entrance slit one has two degrees of freedom: f_{cy} and d . To calculate f_{cy} vs d one can use Figure 2.3.

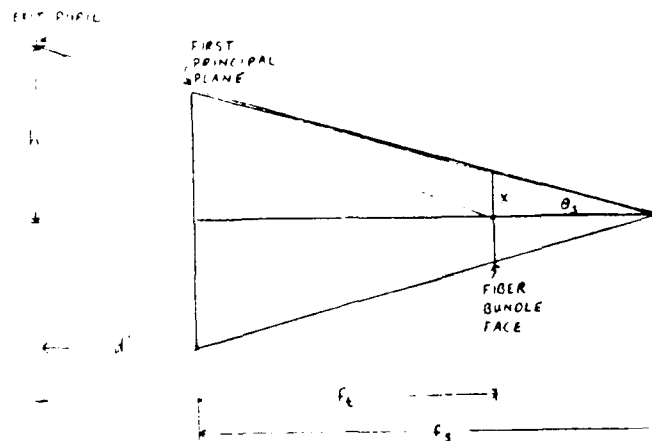


Figure 2.3. Notation used in f_{cy} vs d calculation.

By similar triangles

$$\frac{h}{d' + f_s} = \frac{x}{f_s + f_t} \quad (2.18)$$

so that

$$\frac{1}{f_s} := \frac{h - x}{x \cdot d' - h \cdot f_t} \quad (2.11)$$

combining this with equations 2.9 and 2.10

$$\frac{1}{f_{co}} + \frac{1}{f_{cy}} - \frac{d}{f_{cy} \cdot f_{co}} := \frac{h - x}{x \cdot d' + h \cdot f_{co}} \quad (2.12)$$

and solving for f_{cy} , we find:

$$f_{cy} := \frac{\left[d - f_{co} \right] \cdot \left[x \cdot d' + h \cdot f_{co} \right]}{x \cdot \left[f_{co} + d' \right]} \quad (2.13)$$

In Equations 2.10 through 2.13, d' is the distance between the exit pupil of the copy lens and the second principal plane, h is the radius of the exit pupil of the copy lens, and x is the radius of the paraxial image, formed without the cylindrical lens.

In these calculations two things are assumed. First, the cylindrical lens must be placed in front of the copy lens. This is advisable since for most cases the image from

the fisheye must be reduced, rather than enlarged and therefore, there is more room in front of the copy lens than behind it. Second, f_{cy} is negative. The system can be designed with f_{cy} either positive or negative, but in the positive case a stronger lens is required. It was assumed that a weaker cylindrical lens was desirable to keep aberrations to a minimum.

If one has access to the surface data for the fisheye and copy lens, one can further refine the design. By conducting some computer ray tracing one could vary the surface curvatures of the cylindrical lens and its glass type, rather than just stating a focal length. Here one has four degrees of freedom rather than two with which to minimize aberrations.

We selected a Melles-Griot $f = -80$ mm plano-convex cylindrical lens. The lens was 60 mm wide by 31 mm long. The $f = -80$ mm lens was selected because of its large size and that it was a stock item.

Field Lens

The purpose of a field lens is to reduce vignetting. It is placed at the intermediate image behind the fisheye lens. It takes the light from an off-axis image point and

redirects chief and marginal rays² toward the optical axis, but does not effect final image size, location, or orientation. This is illustrated in Figure 2.4.

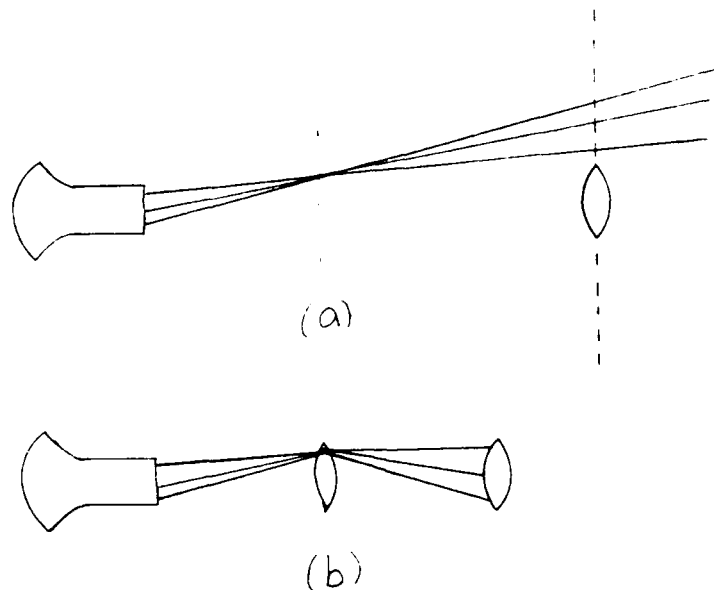


Figure 2.4. Effect of the field lens. (a) The chief and marginal rays from the fisheye miss the copy lens entirely. The dashed line represents the copy lens extended. (b) The chief and marginal rays pass through the copy lens.

The focal length of the field lens is chosen to image the exit pupil of the fisheye onto the entrance pupil of the copy lens (3:213). The focal length of the field lens is determined by the gaussian lens formula. Since the field lens is located at the intermediate image location and the

²For the purpose of this thesis, a marginal ray is defined as a ray from the source that passes close to the aperture stop. This differs from the standard definition which applies to rays starting on the optical axis

pupil locations are also fixed, there are no degrees of freedom in selecting the focal length of the field lens. A lens of diameter larger than the size of the intermediate image should be chosen. When the proper focal length is chosen the chief ray will go through the center of the fisheye exit pupil and the copy lens entrance pupil. That is to say that, barring pupil aberrations, the cone of light will not move in the plane of the copy lens entrance pupil as AOA is changed.

Based on the calculations outlined above a focal length of 51 mm was appropriate, however, a lens with this focal length was not available. We therefore selected a Melles-Griot 80 mm achromatic doublet for the field lens. The 80 mm lens had the shortest focal length on hand and a 31.5 mm diameter which was larger than the intermediate image size. The effect of using an improper focal length is discussed in Chapter III.

Fiber bundle

The primary purpose of the fiber bundle is to transfer the image from the back focal plane of the entrance optics to the plane of the entrance slit. This provides the flexibility to remotely mount the spectrometer, detector, and electronics.

One of the primary design parameters of the fiber bundle is the numerical aperture (NA). The NA of the fiber is related to the $f/\#$ of the cone of light it transmits (Equation 2.15).

$$f/\# = 1/(2 * NA) \quad (2.15)$$

The $f/\#$ of the fiber should be smaller than that of the spectrometer otherwise the grating would be underfilled. It should also be small enough to accept light from all objects in the field of view. This can best be seen in Figure 2.5.

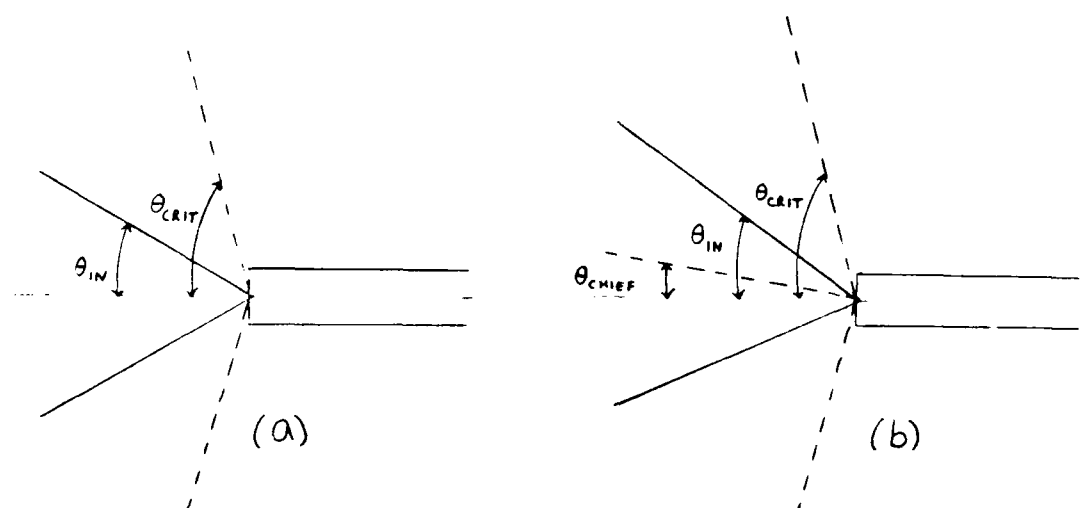


Figure 2.5. Effect of off-axis objects on fiber $f/\#$. (a) on-axis. (b) off-axis.

For an on-axis object, $(f/\#)_{in} \approx (f/\#)_{fiber}$ is sufficient. For off-axis objects, i.e. objects whose AOA is not zero, the cone of light from the copy lens will be skewed. The cone of light the fiber will accept must be large enough to accept all the incoming light, otherwise vignetting for off-axis objects will result.

A second design parameter is the diameter of the core of the individual fibers. The fiber bundle effectively "digitizes" the image on its face. If light from different objects are incident on an individual fiber, the light from both objects will be emitted indistinguishably into a single cone centered on the fiber core. That is to say, all detail smaller than the fiber center to center spacing will be lost. Hence it is advantageous to make the fibers as small as one can before diffractive effects dominate.

There are several other minor design parameters. The bundle face should be larger than the entrance slit. The fiber should be composed of a material that transmits in the wavelength region of interest. The bundle length should be only as long as necessary since these bundles tend to have losses in the tens of percent per foot. The transmission curve must be known if the system is to measure pulse energy accurately (see Measuring Pulse Energy, this chapter).

The number of firms that produce these coherent fiber bundles are few. While length and size are made to order,

the core diameter and numerical aperture seem standard. We bought a bundle from Applied Fiberoptics, Inc. which had 10 micron diameter cores and a numerical aperture of .66. The face was 4 mm X 8 mm and the bundle was 1.3 m long. The selection of Applied Fiberoptics, Inc. was based on cost and delivery time.

Neutral Density Filters

The system can be operated with the detector saturated or not, with either approach involving several trade-offs. The decision to saturate or not must be based on what threat data the user needs.

If the system is run "wide open," very weak sources can be detected and their pulse energy measured. However, for monochromatic sources other than very weak ones, the detector will saturate. When this occurs one can only say that the pulse energy is greater than some value, and not what it actually is. One also must be careful about the blooming characteristics of the detector. A comparison of the blooming characteristics of the CCD and CID detectors can be found in Chapter IV.

If determining pulse energy is the priority, one can take measures to reduce the throughput to avoid saturating the detector. This is done by stopping down the system and thereby center the detector's operating range on the

anticipated pulse energy. This, however, raises the system MED. The system can be stopped down in several ways. First, one can reduce the width of the entrance slit. In addition to stopping down the system, this will increase the wavelength resolution of the system. Second, one can stop down the fisheye lens. This will reduce vignetting for off-axis objects as well as reduce system throughput. Third, one can introduce neutral density filters somewhere between the fisheye and the fiber bundle face. Finally, one can choose a cylindrical lens to produce a longer than necessary focal line. This has the added advantage of providing a more uniform response for objects at the edge of the field of view. One does not want to stop down the copy lens as this will increase vignetting for off-axis points if the field lens is in any way misaligned.

We used a 100 micron entrance slit which gave us adequate resolution without sacrificing the MED. The fisheye lens was wide open in virtually all cases as vignetting was not a problem. We changed the neutral density filters to adjust the operating range of the detectors as needed.

In most cases, background light will not be a factor in this system if it is non-monochromatic. The energy from monochromatic light is concentrated on a small part of the detector. Whereas energy from non-monochromatic sources is

dispersed over several hundred pixels. Because of this, if two sources of equal irradiance are incident on the fisheye and if one is monochromatic and the other isn't, the monochromatic one will appear two orders of magnitude "brighter" than the other. Hence, one tends to adjust system throughput based on the intended threat and not on the solar background.

Extending the Useable Range Through 1.06 microns

One might be tempted to extend the range of the system to cover from 400 nm to 1100 nm so Nd:YAG radiation could be detected. While this is feasible, the trade-offs in performance would be severe. To implement this change one has two options: either make the detector larger or increase the dispersion of the spectrometer.

If one decides to increase the size of the detector, it can be done in one of two ways. If the number of pixels is held constant, but their width increased, the wavelength range covered by each pixel will increase. Hence, the wavelength resolution will decrease linearly with the increase in wavelength range. If the width of the pixels is held constant, but their numbers increased, then the system will run slower and the detector will be more expensive. This decreases the maximum prf discernable.

If one decides to increase the dispersion, this can be done by decreasing the focal length of the spectrometer or the groove density of the grating. Either will increase the wavelength range covered by each pixel and decrease the wavelength resolution. It should also be noted that when the commercially available spectrometer with the shortest focal length is matched to the commercially available aberration corrected holographic grating with the least groove density (as was done in the experimental portion of this thesis), the dispersion is still too low to cover 400 nm - 1100 nm when using the largest commercially available CID detector. Hence, a custom designed and manufactured spectrometer or grating would be required.

Regardless of how it is done, changes are required to deal with overlapping orders. The 800 nm - 1100 nm range for the first order would overlap the 400 nm - 550 nm range for the second order. One can determine which frequency is present by checking for corresponding peaks in the first and second orders in the 400 nm - 550 nm range.

If one is interested in a 400 nm wavelength range, there is some flexibility in choosing the center wavelength without changing hardware. Changing the central wavelength from 600 nm to 750 nm, for example, simply requires a lateral shift in the detector mounting. The absolute wavelength range is limited to between 400 nm and 1100 nm by

the responsivity of the silicon in the detector and may be further restricted by the particular spectrometer used. The problem of overlapping orders still must be dealt with, however.

We opted not to extend the range through 1.06 microns. One of the basic assumptions of this thesis was that the radiation to be detected was in the visible range. The sacrifices in system performance required to extend the range were too severe to justify.

Measuring Pulse Energy

The system's output for a given pulse energy input varied with AOA and wavelength (1). This occurred for several reasons. First, the detector's quantum efficiency is strongly wavelength dependent. Second, the detector, being a photon counter, must have its response adjusted by $E = hf$ to provide a measure of energy. Third, the entrance optics experience vignetting for large values of AOA. This can be minimized by careful selection and alignment of a field lens, but cannot be altogether eliminated since it is inherent in the fisheye. Fourth, the transmission characteristics of the fiber bundle drop off sharply below 500 nm. Fifth, the effective entrance pupil area has a general $\cos(\text{AOA})$ dependence. Lastly, the cylindrical lens, which produces a line of light that does not have a uniform

energy distribution along it, adds another AOA dependence. The net effect of these factors is that both the calibration of pulse energy from detector response and the MED have strong non-linear AOA and wavelength dependencies.

Maximum Pulse Repetition Frequency (prf) Discernable

The maximum prf discernable depends only on the frame rate of the detector. For a pulse train consisting of only a few pulses, a prf equal to half the frame rate is the highest that can be measured. For a prf greater than the frame rate, the detector will interpret several weak pulses as a single strong one. In this case, the data reported by the detector is more accurately interpreted as an average irradiance, rather than pulse energy per unit area. The maximum frame rate for the CID we selected was 30 Hz.

Modeling

We attempted to model the entrance optics using CODEV lens design software. We did this to optimize the design thereby achieving the smallest spot size possible. The effort was severely hampered by the lack of lens data on the Nikkor fisheye and the COI copy lens. The only data available to us was spec sheets which included a small mechanical drawing of the lens. From these drawings the surface curvature and thickness of each lens could be estimated. The distance between the lenses could also be

determined. To determine the glass types, we modeled the system with different glasses and compared the results (e.g. front and back focal lengths and entrance/exit pupil location and size) to the vendor's specification sheets. However, since the model prediction had to be so precise, the modelling was not useful. In the future, we would recommend that no modelling beyond the simple geometric optics discussed in the last chapter be attempted without lens data from the manufacturer.

III. Implementation

The previous chapter contained information which was common to the generic design proposed in Chapter I. This chapter contains information which is specific to the equipment we used in performing the experiments. Any data specific to an individual piece of equipment that was needed for system design, provided by the vendor or determined experimentally, is included here. Calibration procedures and testing system level performance factors is reserved for Chapter IV.

The Test Bench

All testing was done on a Newport 4' X 20' isolation table. The layout of components is illustrated in Figure 3.1. A list of the major components is included in Table 3.1. All of the entrance optics (fisheye through copy lens) were located on the optical rail which was mounted to the rotary stage at the center of the table. The test bench used three sources: an arc lamp, a frequency doubled Nd:YLF laser, and a HeNe laser. Test equipment consisted of an energy meter and a radiometer.

The arc lamp consisted of an ORIEL model 66059 arc lamp housing, an OSRAM model XBO 150 W/1 xenon lamp, and an ORIEL

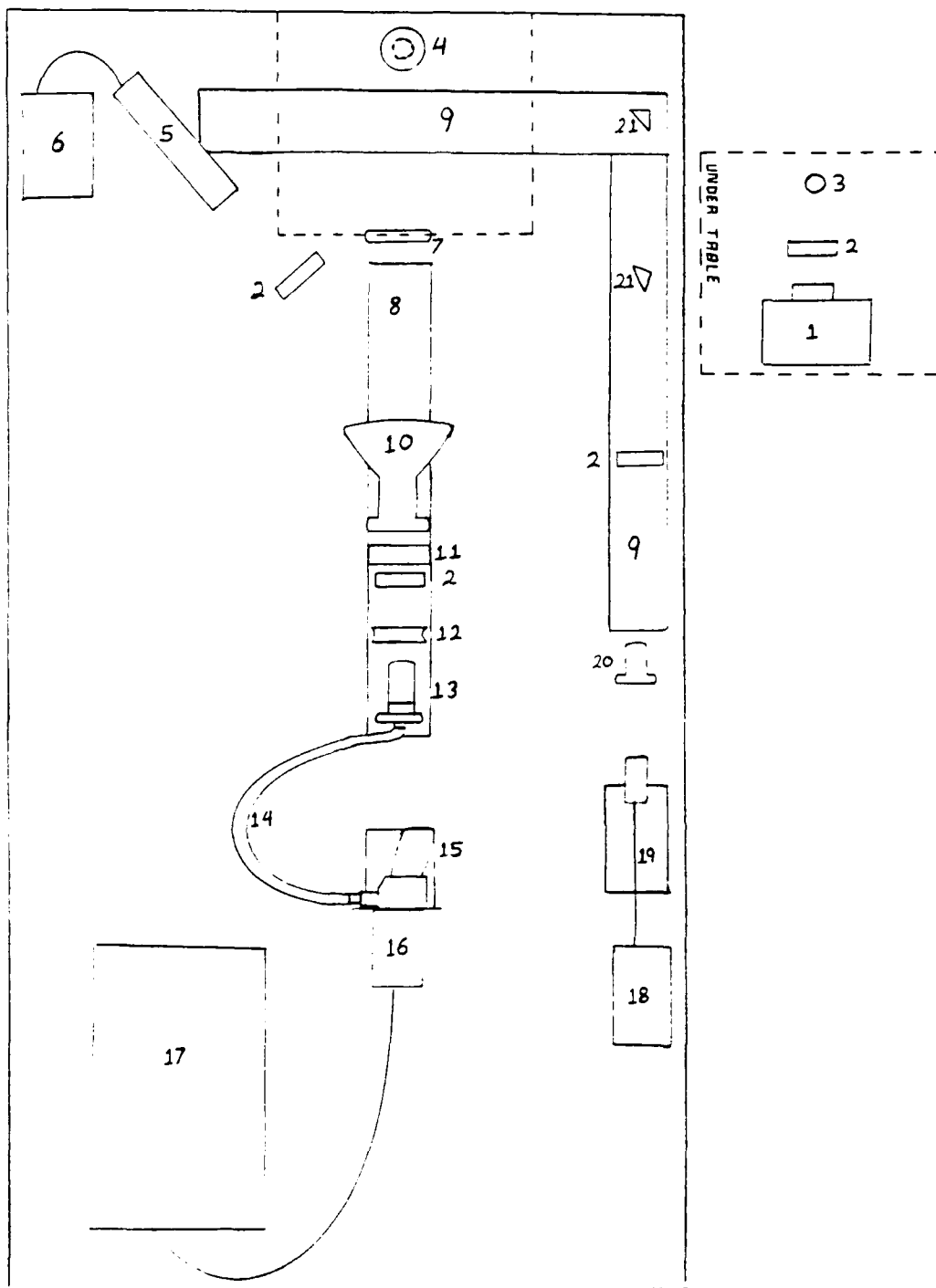


Figure 3.1. Test bench layout.

Table 3.1. Legend for test bench layout

1. Arc lamp housing
2. Filter holder
3. Periscope (lower)
4. Periscope (upper)
5. HeNe laser
6. HeNe power supply
7. Adjustable iris
8. Optical Rail (rotary stage mounted)
9. Optical Rail (table mounted)
10. Fisheye lens
11. Field lens
12. Cylindrical lens
13. Copy lens
14. Fiber bundle
15. Spectrograph housing
16. Detector
17. Detector controller
18. Nd:YLF power supply
19. Nd:YLF laser
20. Beam expander
21. Turning mirror

model 68806 50-200 watt power supply. It produced a collimated five cm diameter beam with an irradiance of approximately 4.5 mW/cm^2 . The housing and lamp were mounted on an aluminum plate on the floor, under the table. Also mounted on the plate was a filter holder, the lower half of a periscope, and an adjustable iris. Mounted to the table, above a hole in the table, was the upper half of the periscope. There were two more irises on the table: one over the hole, the other rod mounted.

The HeNe laser had a COHERENT model CR-40-20H head and COHERENT model 0156-246-00 power supply. It was expanded and collimated by a Melles-Griot model 09-LBM-017 30 X Beam Expander. The expanded beam had an irradiance of approximately 1.8 mW/cm^2 .

The frequency doubled Nd:YLF was produced by Spectra-Physics and was diode pumped. It used a model 7200 laser Diode Module, a model 7250 Q-switch Driver, a model 7950 Q-switched Laser Head, and a model 7955 Frequency Doubler. It emitted at 523.5 nm and had a pulse repetition frequency (prf) that varied from 10 Hz to 10 KHz. It was expanded and collimated by a Melles-Griot model 09-LBX-003 10 X beam expander. The resulting beam was approximately one cm in diameter at the $1/e^2$ power points. The energy per pulse varied with the prf and was plotted in Figure 3.2.

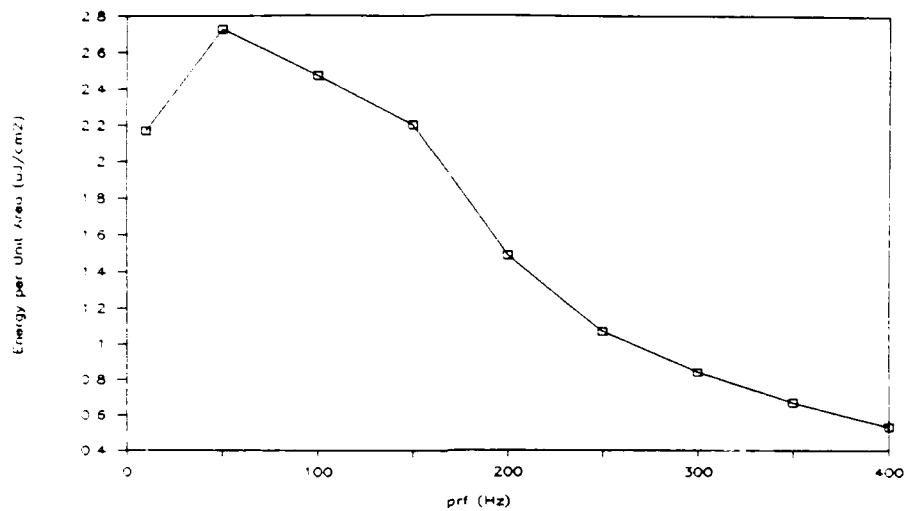


Figure 3.2. Pulse energy vs prf (Nd:YLF).

Energy measurements were made by a Laser Precision Corp model RjP-765 energy probe. The RjP-765 had a 1 cm^2 silicon detector. The probe was set to provide a gain of $2.5 \times 10^6 \text{ V/J}$ and had a quantum efficiency of .30 at 525 nm. The voltage spikes produced by the probe were read by a Tektronix model 2465A oscilloscope. Equation 3.1 was used to convert the peak amplitude (volts) to pulse energy (J/cm^2).

$$E = V / (G * A) \quad (3.1)$$

Here, E is the pulse energy per cm^2 , V is peak amplitude, G is the gain, and Q is the quantum efficiency.

Detector

As was stated earlier, this experiment used two different detectors: an EG&G model 1430-P CCD array and a CIDTEC model 2250A4 CID array. The primary reason for testing both detectors was to quantify the blooming characteristics of each and its effect on system performance factors. Any differences which were due to the hardware or software driving the detectors was discounted or otherwise noted as they are out of the scope of this thesis.

CCD Array. The EG&G model 1430-P CCD array was designed for spectroscopic applications. The exposure time was controlled by a mechanical shutter which could be set from 50 ms to several minutes or hours. It also used a 3-stage Peltier cooler to provide an operating temperature between -10°C and -60°C . This necessitated the use of water cooling and gaseous nitrogen purge lines. Hence, for a laser warning receiver the 1430-P is unacceptable.

The 1430-P was adequate, however, for a lab mock-up if certain precautions are followed. Since most measurements were done on individual frames of data, the shutter speed was set to coincide with a given frame rate. For example, a shutter speed of .1 sec corresponded to a frame rate of 10 Hz. Second, those measurements involving thermal noise, such as the Minimum Laser Pulse Energy Detectable (MED),

were discounted or modified. When the effects of the shutter and the cooling are taken into account the 1430-P can be used for the majority of experiments in Chapter IV.

The 1430-P used a Thompson CFS model TH-7882 CCD. It has a 576 X 384 array of square pixels with 23 microns between centers. This made the overall dimensions of the detector 13.25 mm wide by 8.83 mm high. Since the entrance slit is only 6 mm high, only the middle 260 rows of the detector were actually used. Each pixel had about an 80% fill factor (percentage of format size available for charge collection). Detector responsivity cut off at 400 nm and 1100 nm and peaked at about 600 nm, as shown in Figure 3.3. The CCD clocked out horizontally and did not use 2:1 interlacing. It was not RS-170 compatible.

The 1430-P was driven by an EG&G OMA III model 1460 detector console and an EG&G model 1430-1 detector controller. The OMA III allowed single frames of data to be taken and the value of individual pixels to be determined. It had an A/D converter which divided the usable range of the detector into 16384 (2^{14}) levels.

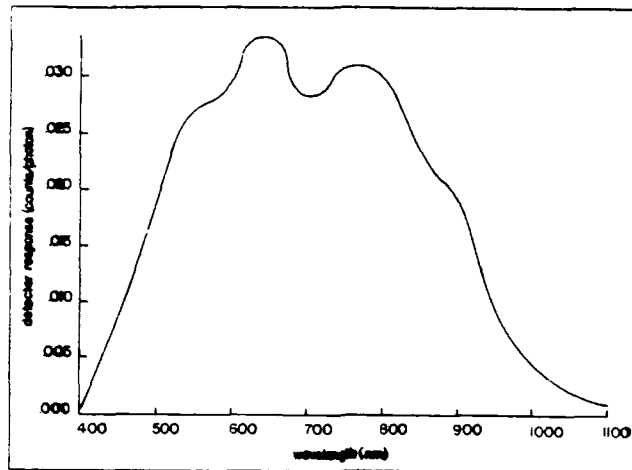


Figure 3.3. CCD detector response.
(courtesy of EG&G Princeton Applied Research, Inc)

CID Array

The CIDTEC model 2250A4 CID detector had a 512 X 512 array of square pixels with 15 micron center to center separation. This made the overall dimensions of the detector 7.68 mm square. Since the entrance slit was 6 mm high, only the middle 400 rows of the detector were actually used. The CID did not use 2:1 interlacing and was not RS-170 compatible.

The CID detector was driven by SPIRACON hardware and software. A BL-2250 frame grabber in an IBM AT PC with a 10 MHz clock rate was used. The SPIRACON allowed for a variable frame rate from 1 Hz to 30 Hz. As with the OMA III, the SPIRACON system was used primarily to grab a single frame and read the values of individual pixels. It had an

A/D converter which divided the usable range of the detector into 512 (2^9) levels.

Spectrometer

The CP-200 spectrometer had a 200 mm focal length and operated at $f/3$. A sketch of the instrument is provided in Figure 3.4.

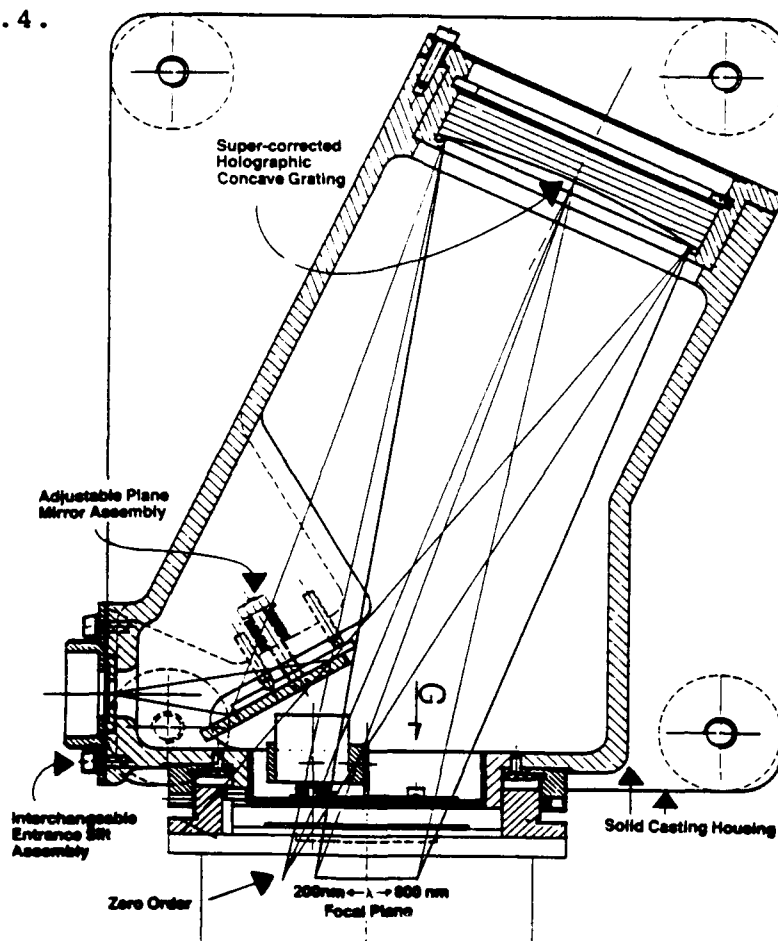


Figure 3.4. CP-200 spectrometer.
(courtesy of Instruments S.A. Inc)

The CP-200 had a 133 g/mm circular holographic grating that was 70 mm in diameter. The focal plane of the

instrument was approximately 11 mm past the detector mounting plate. The focal plane had a useable area of 6 mm X 25 mm. This is wider, but not as high as either of the detectors, so only 260 rows on the CCD and 400 rows on the CID were actually used. Three entrance slits were supplied with the CP-200: 50 micron, 100 micron, and 250 micron. All three were 6 mm high. For the tests reported in this thesis, the 100 micron slit was used. The detector mounting plate was connected to the spectrometer housing by a rotating ring that allowed a ± 2 mm movement of the detector about the focal plane.

Two modifications were required to the CP-200 for its use in this experiment. First, the entrance slit holder was replaced by an aluminum cube approximately 60 mm on a side. Through the middle of this cube a hole was bored 46 mm in diameter. The fiber bundle end was mounted in this hole and held in place by a set screw. Second, the stock mounting plate was too small in diameter for the 1430-P CCD to be attached. The mounting plate was extended with an aluminum plate which was attached with epoxy.

Originally it was planned to simply butt the face of the fiber bundle up against the entrance slit. This was found not to work, because the actual entrance slit was recessed approximately .6 mm into its holder. A sharp focus

could not be found on the detector with this configuration. To remedy the situation, the 100 micron entrance slit was carefully removed from its holder and attached to the face of the fiber bundle with tape. The bundle was then reinserted to a point .6 mm deeper than it was originally.

Several calculations on the CP-200 were made. Two primary calculations, one relating column number (x), to wavelength (λ), and the other relating row number (y), to AOA, are in Chapter IV. These calculations are in Chapter IV so that the calculations, calibration, and testing for a given performance factor are all in the same section. Two calculations, dispersion and bandpass, are included here. All the calculations rely on vendor supplied data, but the final results were tested experimentally and are reported in Chapter IV.

The bulk of the equations were taken from "Optics of Spectroscopy, A Tutorial V2.0" by J.M. Lerner and A. Thevenon. The notation is not standard and so is provided in the Figure 3.5.

$$\Gamma := \text{atan} \left[\frac{HB_L - d}{L_H} \right] \quad (3.2)$$

$$b_L := b_H - \Gamma \quad (3.3)$$

$$\frac{dl}{dx} := \frac{\cos(b) \cdot \cos(\Gamma)^2}{k \cdot n \cdot L_H} \quad (2:EQN 1-8)$$

(3.4)

Given these equations and the values for constants given above, Figure 3.6 was made.

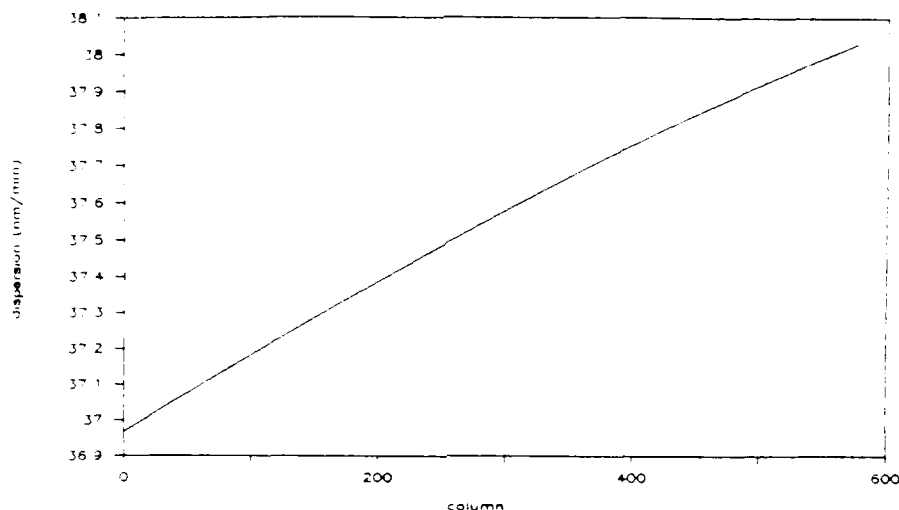


Figure 3.6. Dispersion vs column number.

The dispersion (Equation 3.4) was multiplied by the size of the image of the entrance slit (Equation 3.5) to give the bandpass (Equation 3.6).

$$\text{width of image of entrance slit} = \frac{\frac{LB}{A} \cos(a)}{L \cos(b)} \cdot w \quad (2:EQN 2-16) \quad (3.5)$$

$$BP := \frac{\frac{LB}{A} \cos(a) \cdot \cos(\Gamma)^2}{\frac{LB}{A} \cdot k \cdot n \cdot \frac{L}{H}} \quad (3.6)$$

In Equations 3.5 and 3.6, w is the entrance slit width. A plot of bandpass for the CP-200 is given in Figure 3.7.

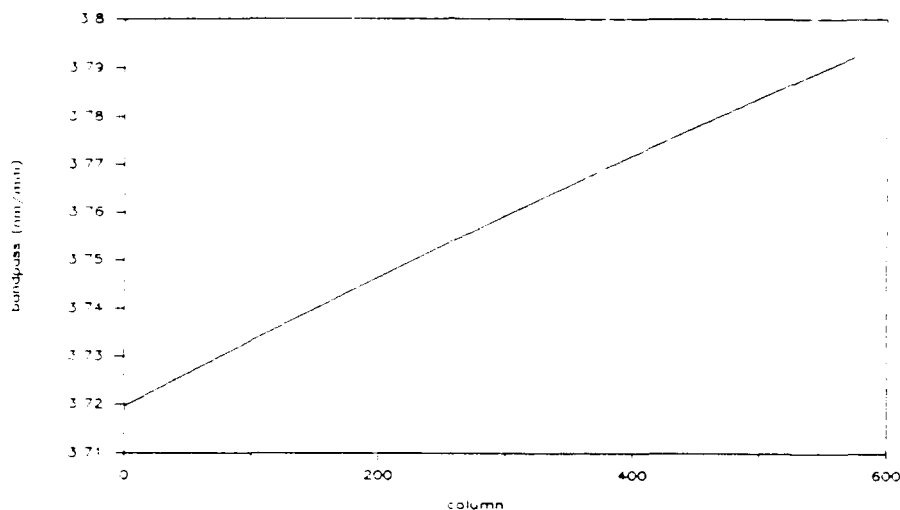


Figure 3.7. Bandpass vs column number.

Fisheye Lens

The Nikkor 8 mm f/2.8 fisheye consisted of ten lenses in eight groups. A mechanical drawing of the fisheye is provided in Figure 3.8.

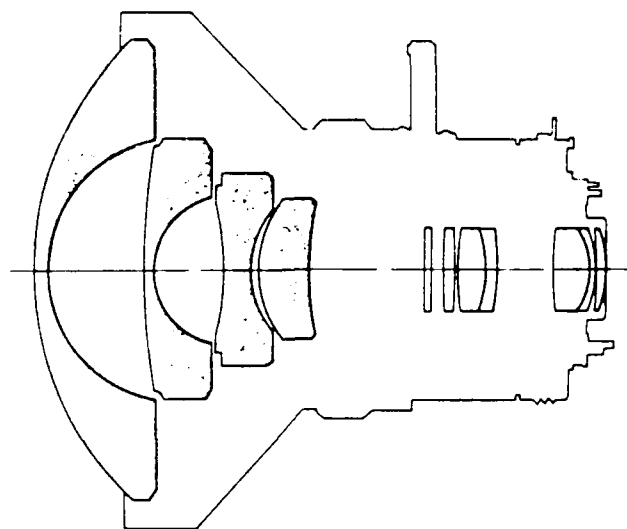


Figure 3.8. Fisheye lens.
(courtesy of Nikkor Corp)

The fisheye was operated at $f/2.8$ and focused at infinity. The fisheye had a built-in filter wheel and the L1BC (skylight) filter was used in all tests. The 8 mm focal length gave the fisheye a 23 mm diameter image with a circular format in the back focal plane. The back focal length was 37.6 mm. The exit pupil was 63.5 mm from the back focal plane and 22.7 mm in diameter.

The linearity of the image height (H) vs AOA relation was tested using a millimeter ruler and the arc lamp. The ruler was mounted on an index card such that it could be positioned anywhere on the optical rail without deviating

horizontally. To test the linearity, the AOA of the arc lamp beam was varied and the location of the spot in the focal plane recorded. The accuracy of the test was limited by the scale of the millimeter ruler. A plot of H vs AOA is given in Figure 3.9.

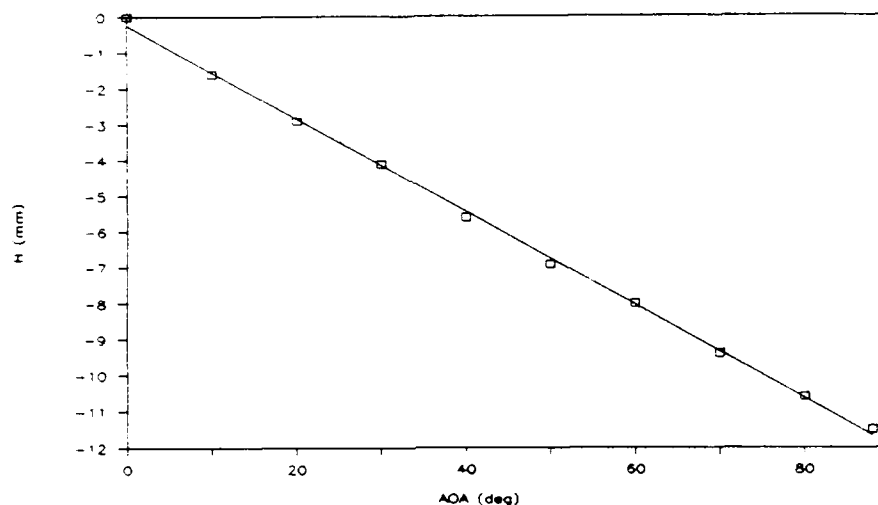


Figure 3.9. H vs AOA for the fisheye.

One characteristic of fisheye lenses is that the entrance pupil changes location and size with AOA. This characteristic was tested using the arc lamp. With AOA = 90° the fisheye was moved along the optical rail until the entrance pupil was centered on the arc lamp beam. The fisheye's position on the optical rail was marked. For several different AOA's, the positioning process was repeated and the displacement of the fisheye from its

original position (D_x) recorded. A plot of the results is given in Figure 3.10.

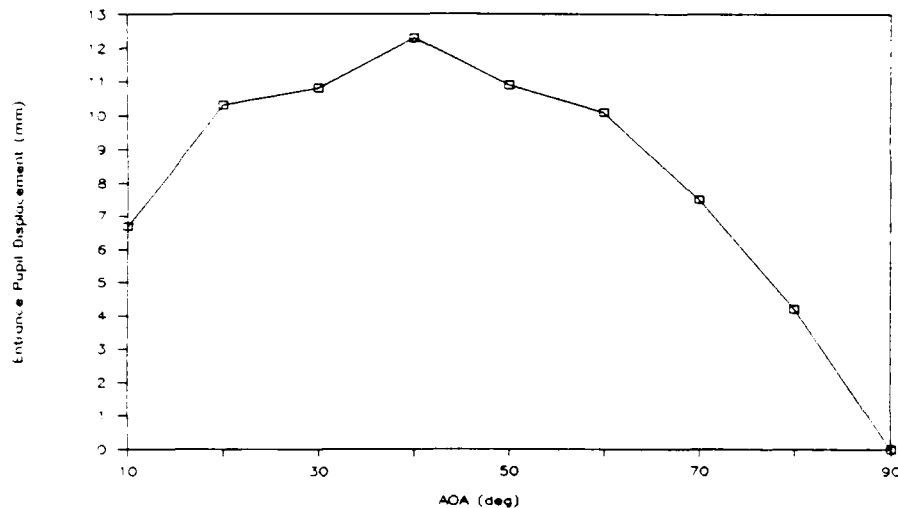


Figure 3.10. Displacement of entrance pupil vs AOA.

The fisheye was positioned at $D_x = 8$ mm, which was a medium position, and left there for all system tests. The net effect was a minor AOA dependence in the location of the entrance pupil. The effects of this on the test program were minimized by the large size of the arc lamp and laser beams.

Field Lens

The field lens used in this experiment did not have the appropriate focal length. According to vendor data, the distance between the fisheye exit pupil and the intermediate image plane was 65.7 mm the entrance pupil of the copy lens

was 37.4 mm past the first surface of the copy lens. This made the distance between intermediate image plane and the copy lens' entrance pupil 270.2 mm. With the gaussian lens equation, the optimum focal length was found to be 51.15 mm. We used a focal length of 80 mm. This was done because a 51 mm lens was not available and the 80 mm was the doublet with the shortest focal length available. The net effect was that the fisheye exit pupil was not imaged precisely onto the copy lens' entrance pupil. This resulted in a somewhat lessened, but still detectable, amount of vignetting with increasing AOA.

To determine the effect of the field lens, measurements were made of the power transmitted vs AOA. These measurements were taken using the arc lamp and the EG&G 450 Radiometer. For these measurements the radiometer's detector was near the back focal plane of the entrance optics. The results are included in Figure 3.11.

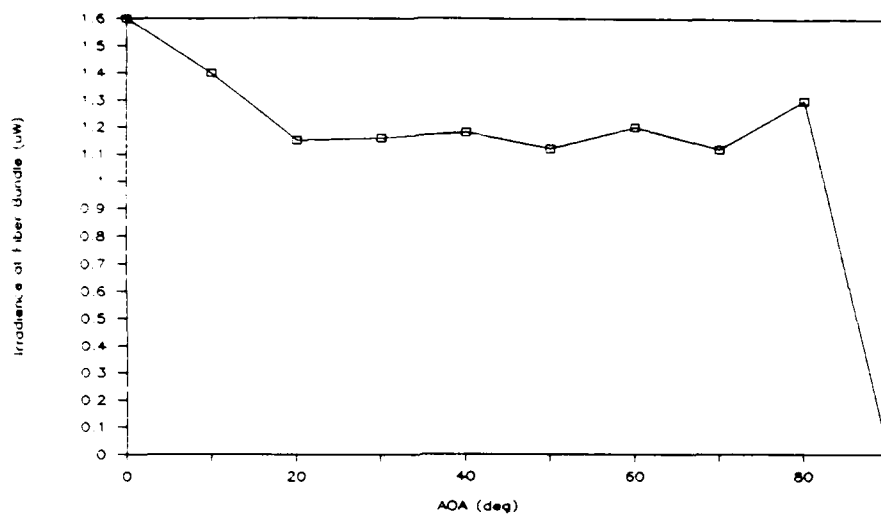


Figure 3.11. Power transmitted vs AOA for entrance optics.

F-Number Matching

It is important to have the core of light from the entrance slit just fill the grating. Underfilling the grating would reduce the resolving power of the spectrometer. Overfilling the grating would increase the amount of stray light in the spectrometer.

The original design of the system relied on the $f/\#$ of the light from the copy lens to match that of the spectrometer. Based on the size of the last element in the copy lens and the distance between the copy lens and the fiber bundle face, an $f/\# \leq 2.8$ was expected. This overly simplistic view was complicated by three factors: the NA of the fiber, the effect of the cylindrical lens, and the angle of incidence for off-axis points.

The fiber bundle manufacturer stated that due to bending of the fiber bundle $NA_{in} \neq NA_{out}$. In general, the vendor stated, the light will emerge from the fiber at its numerical aperture regardless of the NA it was incident with. We did not find this to be the case for the 1.3 m fiber bundle we used. To test this, microscope objectives with different numerical apertures were used to focus light from the arc lamp onto the fiber bundle face. The fiber bundle end was positioned a fixed distance from an index card and the diameter of the resulting disk of light was measured. The results are included in Table 3.2. These results do not confirm the $NA_{out} = NA_{fiber}$ relation stated by the vendor.

Table 3.2. Data for NA(out) measurement of fiber bundle

NA(in)	NA(out)
0.12	0.158
0.25	0.275
0.40	0.33

The cylindrical lens had the effect of making the numerical aperture at the fiber bundle face in the sagittal and tangential planes different. Since a negative cylindrical lens was used, the focal point in the sagittal plane was pushed beyond the fiber bundle face, and the rays struck the face at less of an angle in this plane than they

did in the tangential. Without the fiber bundle, the grating would have been underfilled in the horizontal direction. This problem was avoided because of the randomizing property of the bundle. Light entering a circular fiber in one plane has no bearing on the plane it will be emitted into. Hence, the energy distribution on the grating was shifted toward the center, but all parts were still illuminated.

For off-axis points, the cone of light was not incident normal to the fiber bundle face. The randomizing property of the fiber bundle caused the emitted cone of light to be normal to the fiber bundle end and larger than the input cone. As a worst case assumption, for $AOA = 85^\circ$, the cone was offset by 2.8° , thus decreasing the $f/\#$ from 2.8 to 2.24.

To test the overall effect of these factors background readings were taken using the CCD detector when the arc lamp was at $AOA = 0^\circ$ and at $AOA = 70^\circ$. No detectable change in background was observed.

Alignment

The general assembly/alignment process occurred as follows. First, the system was assembled as described in

Chapter III. Second, the Nd:YLF laser and arc lamp were aligned. Using these sources, the entrance optics were aligned. The focus on the spectrometer was adjusted and the fiber bundle rotation set. Finally, some tests for alignment sensitivity were conducted. Additional details of these procedures are provided below.

The unexpanded beam from the frequency doubled Nd:YLF was aligned level with the bench, eight inches above it, and parallel to the right optical rail. The turning mirrors were set at the proper height and adjusted so the beam retraced its path back to the laser when each turning mirror's rotary stage was set to zero. The beam expander was added to provide a beam one cm in diameter.

The arc lamp was positioned on the floor. Its collimation was tested by shining it on a wall 30 feet away and measuring the size of the central spot. The lower half of the periscope was positioned directly under the hole in the table with a plumb bob. The tilt on the periscope was adjusted so it would come through the center of the hole. The top part of the periscope was centered above the hole. Its tilt was adjusted to provide a beam level with the table top and eight inches above it. With the beam centered on the axis of rotation of the large rotary stage, the beam made an angle of approximately 2° with the long axis of the

table.

The arc lamp produced a bright central spot and a comet-like tail. The central spot was due to the bright spot on the lamp cathode. The comet-like tail was due to the arc between the cathode and the anode. The entrance pupil of the fisheye was small enough that it passed only a small fraction of the central spot and virtually none of the tail. Regardless, a series of baffles were included to reduce light from the tail: one by the lower periscope mirror, one at the hole in the table and one mounted on a post on the table.

The fisheye lens was positioned on the optical rail as described earlier. The fiber bundle face was mounted on a travelling micrometer stage at the end of the optical rail approximately 257 mm behind the back focal plane of the fisheye. The copy lens was mounted with its first surface approximately 150 mm behind the focal plane of the fisheye. These three elements were checked "by eye" for proper height and tilt. The use of an interferometer at this point would have aided in the alignment process. The micrometer stage was adjusted to provide best focus. To check the positioning of the copy lens and fiber bundle, a test was made of H_{fb} vs AOA, where H_{fb} was the displacement of the spot on the fiber bundle face. H_{fb} was measured from the

location where the spot was when $AOA = 0^\circ$. For this measurement, the fiber bundle was replaced with a plastic millimeter ruler. As AOA was changed, H_{fb} of the spot was recorded. By comparing H_{fb} to H , found in the $H(AOA)$ linearity testing, it was estimated that the reduction ratio was .23. This corresponded to a total image height of 5.29 mm, slightly under the 6.0 mm entrance slit size. The accuracy of this measurement was limited by the millimeter scale of the ruler. A more accurate measure of the reduction ratio was made during the $AOA(y)$ calibration using the CCD array. This procedure is described in Chapter IV. Here the reduction ratio was found to be .2426 for a 5.580 mm image size on the fiber bundle.

The cylindrical lens was positioned to provide a focal line whose length was approximately 5.0 mm. This was found by sliding the cylindrical lens up and down the rail and measuring the length of the focal line with a ruler. This placed the first surface of the cylindrical lens 100 mm behind the focal plane of the fisheye. The height and rotation of the cylindrical lens was checked by eye. As a final check a pen light was placed directly above the fisheye, pointing straight down. Part of the focal line from the penlight still crossed the center of the fiber bundle.

The field lens was positioned next. According to vendor data, the first principal plane was located 1.3 mm inside the doublet. By measuring the distance between surfaces, the field lens was positioned so that the first principal plane was placed at the focal plane of the fisheye. Rotation and height were checked by eye.

As a final step in the optical rail alignment, the micrometer stage was adjusted to provide the sharpest focal line. The rotation of the fiber bundle within its holder on the optical rail was checked by eye.

By using the 250 micron and 100 micron entrance slits, it was estimated that the width of the focal line was approximately 120 microns at the end of the fiber bundle. With the 100 micron entrance slit attached to the end of the bundle, its long axis perpendicular to the focal line and centered on the bundle, the bundle was inserted into its holder. This provided a source 100 micron by 120 micron to be used for focusing. The bundle was inserted approximately .6 mm past the point where it would butt up against the entrance slit holder. The focusing ring on the spectrometer housing was then adjusted until a spot from the Nd:YLF was approximately circular. A more accurate test of the spot size is included in Chapter IV.

The rotation of the fiber bundle entrance slit assembly at the spectrometer housing was especially critical. If one assumes a 3 mm half height for the image of the entrance slit, a displacement of ± 1 column on the detector of the image of the ends of the entrance slit corresponds to a $\pm 0^{\circ}20'$ rotation of the bundle. To properly adjust the rotation of the bundle, the Nd:YLF and a beam splitter were used. Part of the beam was split off and brought in at $\text{AOA} = 80^{\circ}$. The rest of the beam was brought in at $\text{AOA} = -13^{\circ}$ using the turning mirrors. The rotation of the bundle was adjusted until spots from both legs were centered on the same column of the detector.

With the system assembled and aligned, the effect of defocus on the fiber bundle face was tested. Using the arc lamp as a source, the Full Width at Half Maximum (FWHM) of the spectrum at a wavelength of 562.8 nm was measured as the amount of defocus was controlled by the micrometer stage. A plot of FWHM vs defocus is given in Figure 3.12. The other elements of the entrance optics were tested for tilt, rotation, and position sensitivities. Small changes, i.e. changes in position of one mm, or tilt or rotation of 1° , produced no noticeable changes in the spectrum width.

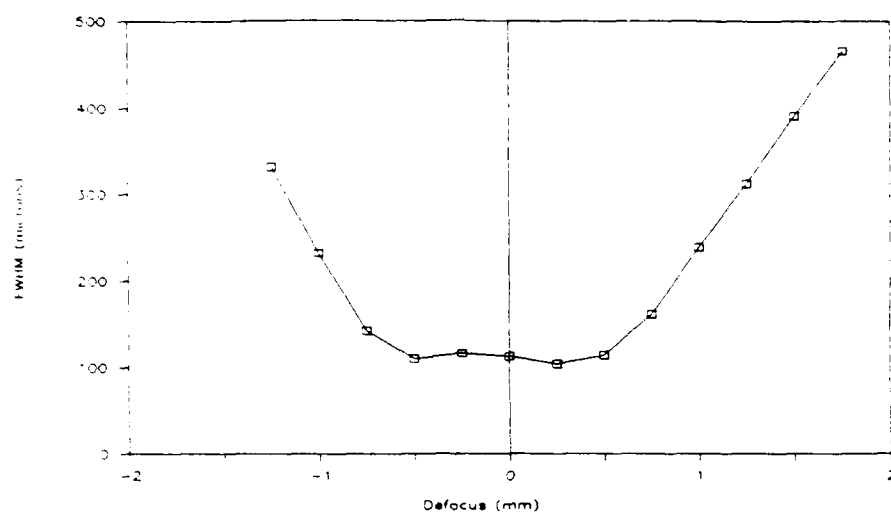


Figure 3.12. FWHM vs defocus of fiber bundle face.

IV. System Testing

This chapter describes the system level calibration and testing conducted using the equipment described in Chapter III. The tests were conducted on the lab bench described in the "Test Bench" section of Chapter III.

Spot Size

The lasers, as monochromatic sources, produced a small, elliptical pattern of light on the focal plane of the detectors, which in this document will be referred to as a "focal spot", or just "spot". The arc lamp, as a broad-band source, produced a line on the detector which will be referred to as the "spectral line" or "spectrum". The size and shape of the spot had a large effect on the accuracy of the wavelength, AOA, and pulse energy measurements.

The arc lamp produced spectral lines with a gaussian cross-section whose width varied with AOA. A plot of spectrum width vs AOA is included in Figure 4.1. The measurements were taken at $\lambda = 526.5 \text{ nm}$. A linear interpolation was used to estimate y for the half power

points. It can be seen that the spectrum widened as the AOA increased. This is to be expected since the point spread function of most lens systems broadens as AOA increases.

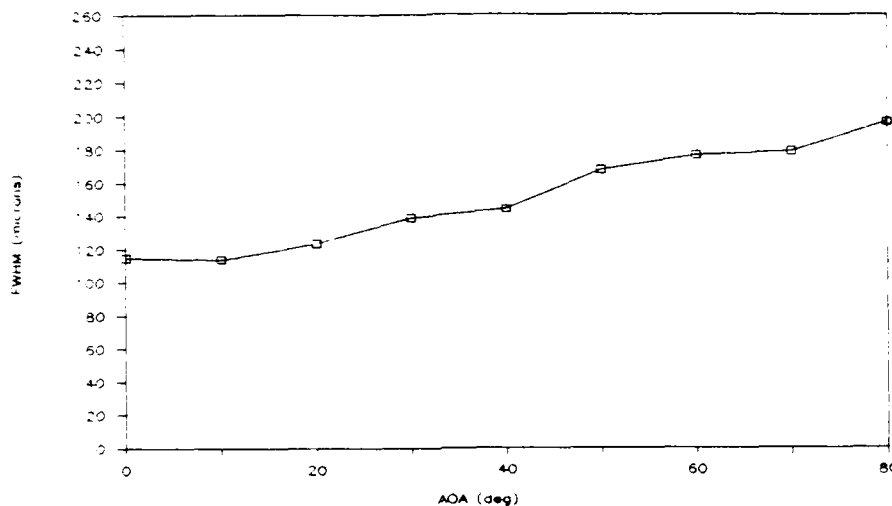


Figure 4.1. Spectrum width vs AOA for the arc lamp.

The lasers produced spots with a bivariate gaussian shape with a correlation coefficient $\geq .99$. Spot size was measured at FWHM in both the x and y directions. Figure 4.2 is a plot of the spot size vs AOA for the Nd:YLF. Spot size varied with AOA, but not in a predictable manner.

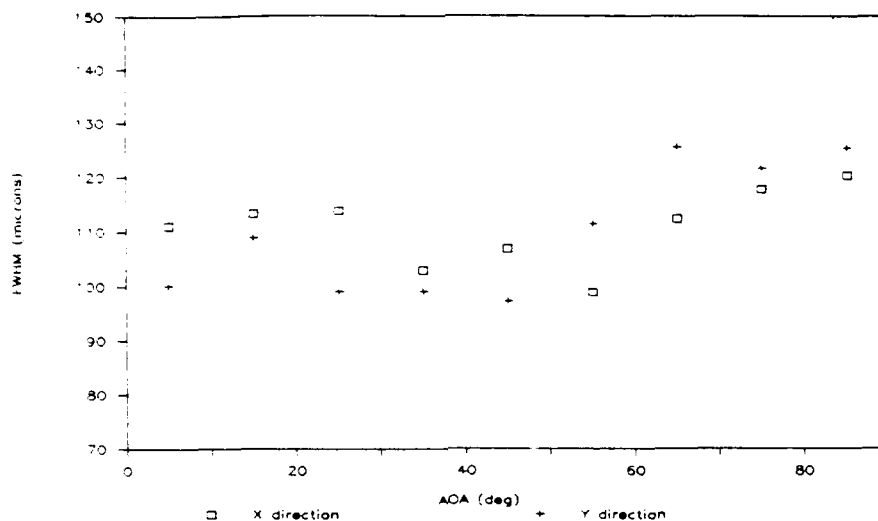


Figure 4.2. Spot size vs AOA for the Nd:YLF.

A test of the change in spot size from frame to frame was made for constant AOA. This test was made using the 100 micron entrance slit and the Nd:YLF as a source at AOA = -2.8. Using a sample size of six, the spot size was 81.42 microns in the y direction with a standard deviation of 6.05 microns. In the x direction the spot size was 107.9 microns with a standard deviation of 1.54 microns. The average maximum count was 3204.5 with a standard deviation of 228.51. The standard deviation of the count could explain the larger variance in the y direction, where the light incident on the entrance slit was not clipped.

Laser sources produced spots that showed some periodic fine structure. The structure was most likely due to an interference pattern caused by the coherence of the laser. It was noticeable on both detectors, but was more prominent using the CID detector. Figure 4.3 is a cross section of a spot taken with the CID detector using the Nd:YLF as a source. The periodic structure was predominantly in the y direction. The structure depended on AOA, but did not vary from frame to frame for constant AOA. It was observed with both the HeNe laser and the Nd:YLF.

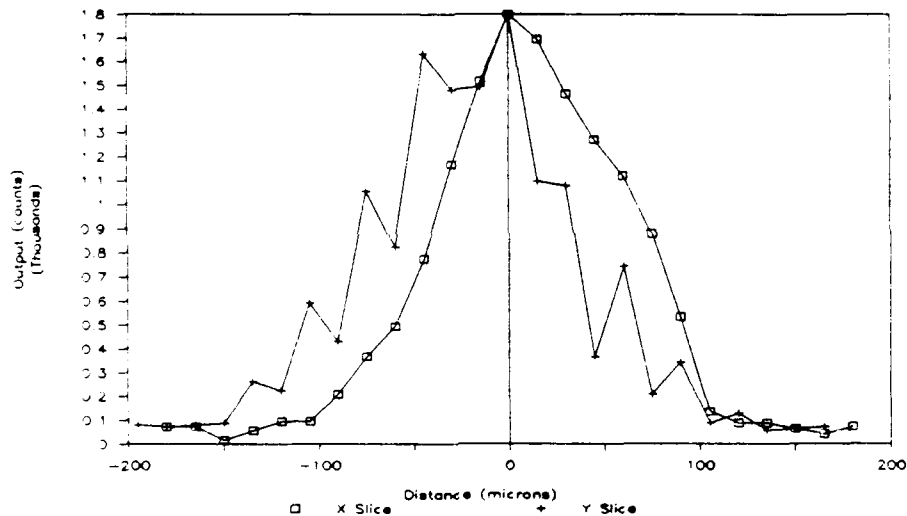


Figure 4.3. X and Y cross-sections of a laser spot.

The existence of a fine structure superimposed on the gaussian was a source of error in the wavelength and AOA measurements. These measurements were made using the pixel with the peak count. The constructive interference of the

fine structure shifted the peak on the gaussian by as much as ± 1 pixel. This error might be reduced by using a gaussian curve fitting routine to estimate the centroid. This error might also be reduced by using a random phase screen somewhere in the beam path to reduce the coherence of the source. In this study, neither method was tested.

Wavelength Measurement Calibration and Testing

Calibration of the detector to determine wavelength was a two step process. First, a general relation between wavelength (λ) and spot location in the focal plane (D) was found using vendor data. Second, a relation between column number (x) and D was found empirically. Combining these two relations, $\lambda(x)$ was calculated. This relation was tested by comparing the predicted x with the experimental, using discrete sources with known spectral characteristics.

The calculation of $\lambda(D)$ was based on the notation given in Chapter III. By combining the dispersion relation (Equation 4.1), and equations derived from Figure 3.5 (Equations 4.2, 4.3, and 4.4),

$$l := \frac{\sin(a) + \sin\left[\frac{b}{L}\right]}{k \cdot n} \quad (4.1)$$

$$D := HB_c - HB_l \quad (4.2)$$

$$HB_l := L_H \cdot \tan\left[\frac{b_H - b_L}{L}\right] \quad (4.3)$$

$$HB_c := L_H \cdot \tan\left[\frac{b_H - b_c}{L}\right] \quad (4.4)$$

$l(D)$ can be derived (Equation 4.5).

$$l(x) := \frac{\sin(a) + \sin\left[b_H - \operatorname{atan}\left[\frac{HB_c - D}{L_H}\right]\right]}{k \cdot n} \quad (4.5)$$

Since a , b_H , L_H , k and n were known and given in Chapter III, Equation 4.5 is only a function of D .

To find a relation between l and x , a relation between D and x was needed, and was assumed to be as shown in Equation 4.6.

$$D := w \cdot x - D_0 \quad (4.6)$$

Here, w is the width of a pixel and D_0 is the horizontal displacement of the detector corresponding to $x=0$.

In Equation 4.7, D was substituted into Equation 4.4.

$$l(x) := \frac{\sin(a) + \sin \left[b_H - \operatorname{atan} \left[\frac{HB - w \cdot x - D_0}{L_H} \right] \right]}{k \cdot n} \quad (4.7)$$

There are two unknowns in Equation 4.7, D_0 and L_H . D_0 is unknown because the detector mounting hardware allows the detector to be shifted horizontally by the user during assembly, and L_H because it was changed by an unknown amount during the focusing process.

The approach taken in calibrating $l(x)$ involved using four pairs of x and l values and finding values of L_H and D_0 to provide a best fit. The sources used and their respective x values are given in Table 4.1. We found the best fit to occur for $L_H = 182.5$ mm and $D_0 = -6.136$ mm. A plot of $l(x)$ predicted by Equation 4.7 and these values is included in Figure 4.4.

Table 4.1. Wavelength Calibration Data

Source	x (col)	Actual Wavelength (nm)	Non-Linear Prediction (nm)	Error (nm)	Linear Prediction (nm)	Error (nm)
Nd:YLF	154	523.5	523.29	0.21	525.3	-1.8
HeNe	281	632.8	632.6	0.2	634.45	-1.65
Xenon arc	501	823.16	823.54	-0.38	823.53	-0.37
Xenon arc	568	881.94	882.05	-0.11	881.12	0.82

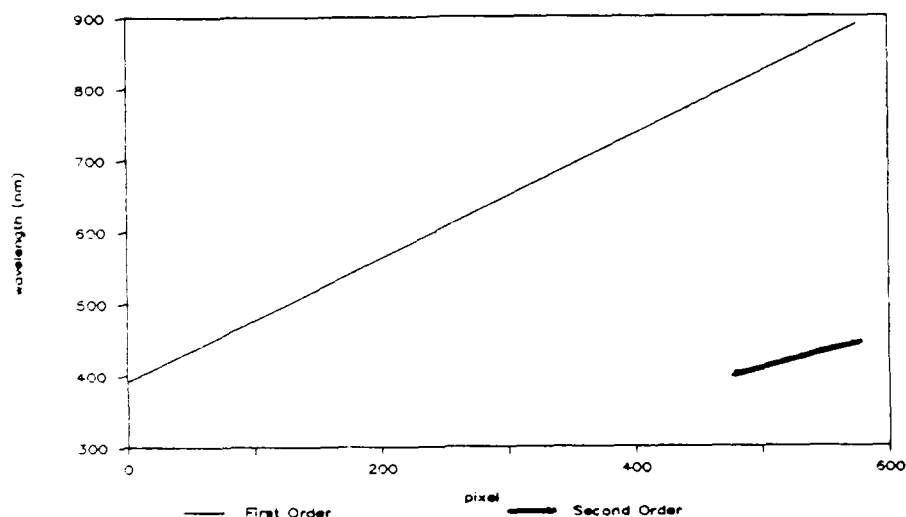


Figure 4.4. Wavelength vs column number for CCD array.

Using Equation 4.7 represented a significant improvement over a linear approximation to $l(x)$. Based on the four data points, the best fit to a straight line occurred when l is found using Equation 4.8.

$$l = .859478x + 392.936148 \quad (4.8)$$

Table 4.1 compares the actual results, results predicted by Equation 4.7, and those predicted by Equation 4.8. Based on these results, the more complex $l(x)$ relation, Equation 4.7, is necessary to obtain a wavelength resolution of ± 1 nm. Table 4.1 shows that the values predicted using Equation 4.7 are within $\pm .4$ nm of the actual value. This test was done at one AOA. A test of AOA accuracy was made using one wavelength (see next section). In this test 14 data points were taken with AOA ranging from 4° to 84° . Of these 14 points, 12 were in the same column and two were in an adjacent column. Since one column corresponds to approximately one nm in wavelength, the more conservative value of ± 1 nm wavelength accuracy may be more appropriate.

Angle of Arrival Calibration and Testing

After alignment and calibration, a test was made to determine the accuracy of the angle of arrival measurement. With the HeNe laser fixed in place and the beam centered on the entrance pupil, the rotary stage holding the optical rail was turned to vary AOA. For each value of AOA tested, a frame of data was taken and the peak value recorded. A total of 14 data points were taken between $AOA = 4^\circ$ and $AOA = 84^\circ$. The y value of the peak was plotted against AOA and is given in Figure 4.5. The correlation coefficient of the 14 data points was $-.9995$. A relationship between y and

AOA was found using a least squares fit and is given in Equation 4.9.

$$y = -1.338675 * \text{AOA} + 198.059 \quad (4.9)$$

For each data point, the difference between the predicted and the actual value was calculated. The standard deviation of the difference was 1.06 rows. This corresponds to an AOA accuracy of ± 40 arc minutes. A plot of y vs AOA is given in Figure 4.5.

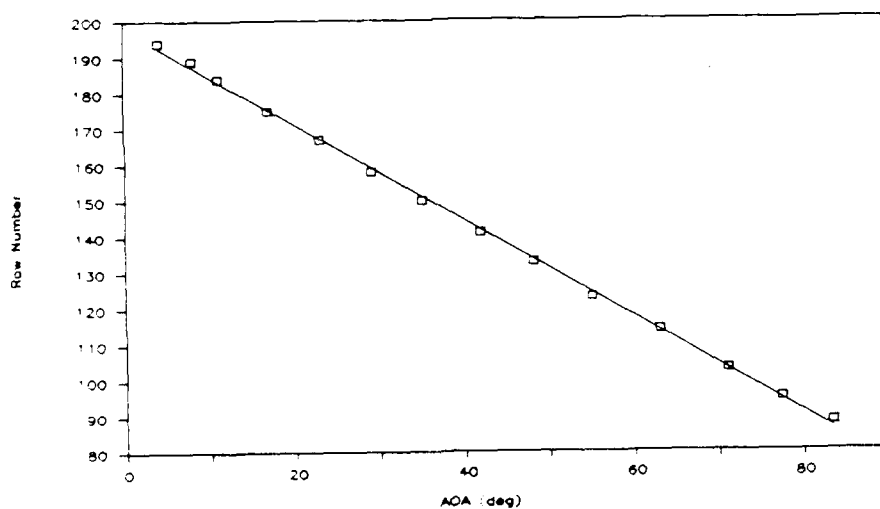


Figure 4.5. Row number vs AOA.

Several things could be done to improve the AOA accuracy. These measurements were taken using the peak value to determine the AOA. As was mentioned in the "spot size" section, using the spot centroid to determine AOA may be more accurate. Using a phase diffuser to remove the fine structure which was the predominant cause of AOA error was also mentioned. Additional accuracy may be obtained if the linear relationship assumed to occur with the fisheye between image height and AOA is replaced with a higher order fit. Overall, however, the ± 40 arc minutes AOA accuracy demonstrated here will most likely be sufficient for a first generation data collection tool.

Pulse Energy Calibration and Testing

An attempt was made to relate the peak count value, z , to the energy per unit area incident on the fisheye. As was described in Chapter III, this relationship has strong AOA and wavelength dependencies. A source with constant pulse energy was used to measure how z varied with AOA for constant λ . The wavelength dependence for constant AOA was found using vendor data. Assuming $z(\text{AOA})$ and $z(\lambda)$ are independent, that the detectors' output varies linearly with input energy, and that all other factors are constant, one can estimate the pulse energy per unit area incident on the fisheye given the peak count value.

The HeNe laser was used to measure $z(\text{AOA})$. Using a 30 X beam expander and an OD 2.2 filter, the HeNe emitted 11.13 uW/cm^2 with a standard deviation of $.11 \text{ uW/cm}^2$. The .1 sec shutter speed on the CCD detector gave the HeNe the appearance of a pulsed source. Fourteen data points were taken. A plot of z vs AOA is included in Figure 4.6.

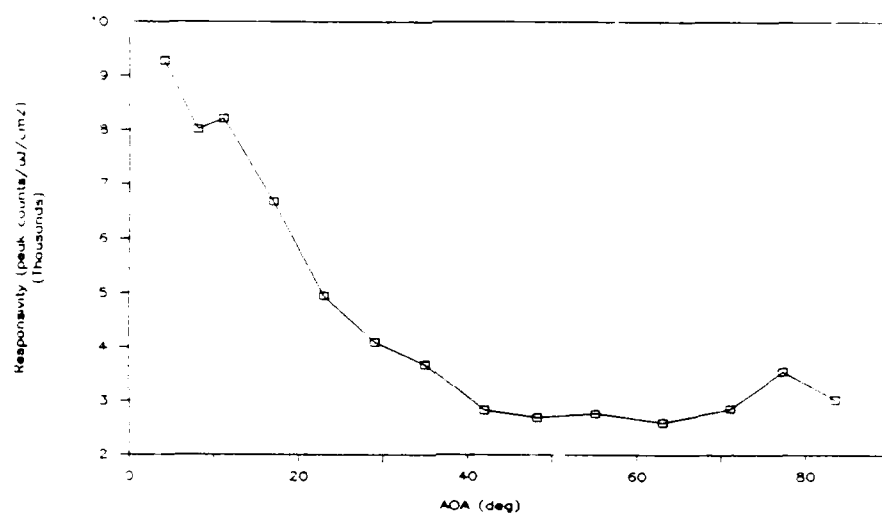


Figure 4.6. System responsivity vs AOA, wide field.

There were several factors contributing to the shape of this curve. The effective area of the entrance pupil and of a detector pixel decreased for off-axis points. This is analogous to the familiar \cos^4 losses in simpler systems. The spot size broadened as AOA increased. This resulted in another loss factor since the energy of the pulse was spread

over more pixels and consequently the peak value dropped.

In calculating $z(l)$ vendor data was used for detector sensitivity (photons/count) and the transmission curve of the fiber bundle. The photon counting nature of the detector also required an $E = hf$ correction. By assuming these factors were independent and in series, a normalized plot of system responsivity vs l was found and included in Figure 4.7.

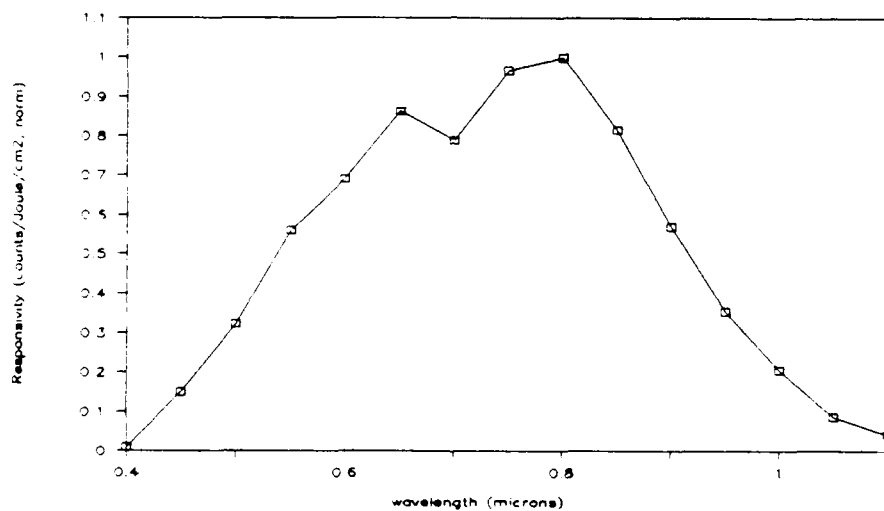


Figure 4.7. System responsivity vs wavelength.

In taking the data for $z(\text{AOA})$ one problem was covered. For very small changes of AOA (arc minutes), relatively large changes in z were detected. These changes could not be explained by the $z(\text{AOA})$ dependence shown in

Figure 4.6. One possible explanation involves the fine structure, or interference, reported earlier in the "spot size" section. As a spot was shifted, the energy on a given pixel would rise and fall according to how many interference peaks were subtended. The net effect would be periodic variation of z when AOA was changed. The use of a random phase screen to control the fine structure interference might reduce this problem, and should be investigated.

A test was made comparing three algorithms for relating z to pulse energy. In the first method, the peak value of the spot was used for z . It resulted in a periodic variation of $\pm 10\%$ in the readings. Second, the spot was fit to a gaussian curve and z_{\max} was interpolated. As a third method, the area under the spot, rather than the peak count, was related to pulse energy. The results of the comparison is given in Figure 4.8. None of the methods completely corrected for the periodicity experienced.

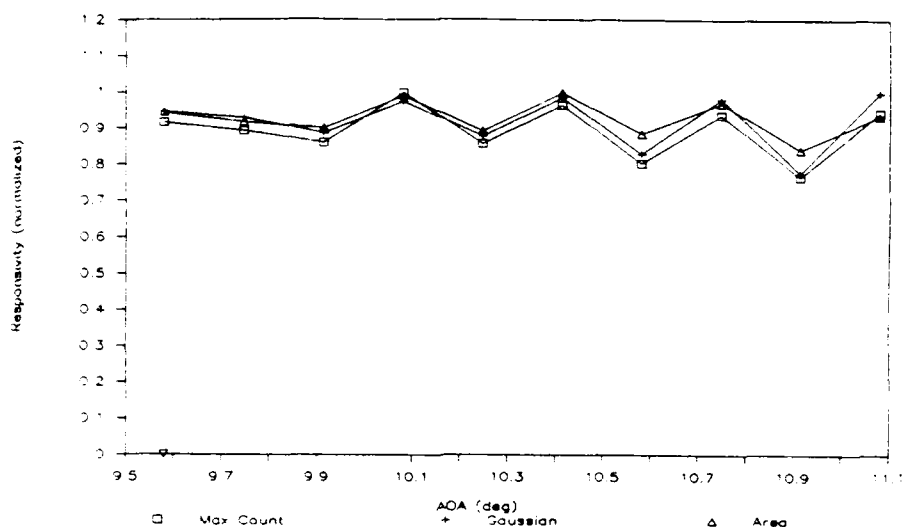


Figure 4.8. System responsivity vs AOA, narrow field.

A measure of the actual losses in the system for one value of AOA and 1 was made. Using the HeNe with the 30 X beam expander and an OD 2.0 filter, a frame of data was taken. The irradiance of the HeNe on the fisheye was 5.1 uW/cm^2 . Of this, $.0327 \text{ uJ}$ of energy got through the $.0641 \text{ cm}^2$ fisheye aperture stop in .1 sec. The total number of counts in the resulting spot was measured at 93524 after the background was subtracted. At 632.8 nm one count equals 31.38 photons, by vendor data, or $9.858 \times 10^{-18} \text{ J}$. Hence the total energy on the detector was $9.219 \times 10^{-13} \text{ J}$. The net result was that for every 35,470 photons incident on the fisheye entrance pupil, one got through the system at

$\lambda = 632.8 \text{ nm}$ and $\text{AOA} = -12^\circ$.

Minimum Laser Pulse Energy Detectable (MED)

Noise Limited Performance. Under the majority of conditions, the detector was thermal noise limited in its performance. To test the MED for the CCD detector, the Nd:YLF was used. With the pulse repetition frequency (prf) set at 10 pps and $\text{AOA} = 45^\circ$, the Nd:YLF put out 2.17 uJ/cm^2 in each pulse. The neutral density filters in front of the Nd:YLF were varied to change the energy at the detector. The shutter speed of the CCD array was set at .1 sec. With the CCD detector cooled to -10° C the background averaged 370.1 counts with a standard deviation of 3.2 counts. Therefore, the target value for a $\text{S/N} = 5$ was 385.6 counts. Readings were taken using an OD of 2.40, 2.60, and 2.80. These OD's were converted to losses and effective pulse energies were calculated. The data had a correlation coefficient of .995. By interpolating, the MED was found to be .28 nJ at 523.5 nm, or $1/22,000$ the Maximum Permissible Exposure (MPE), where the MPE was taken as 6.13 uJ/cm^2 . A similar procedure was used with the CID detector. With the Nd:YLF set at 30 pps and $\text{AOA} = 55^\circ$, the Nd:YLF put out 2.45 uJ/cm^2 per pulse. The CID detector was operated at 30 Hz frame rate and had a 38.72 count background with a standard deviation of 9.98 counts. This gave a target of

88.62 counts for $S/N = 5$. Again, three data points were taken. These data points had a correlation coefficient of .994. An MED was interpolated to be $.132 \text{ uJ/cm}^2$ or $1/45$ MPE.

Background Limited Performance. Due to the vertical separation on the detector, only light from objects within a $\pm 1.25^\circ$ annulus about the target can effect the measurements. Nevertheless, several tests on how the system performed in a solar background outside of this 2.5° annulus were made. These tests were conducted to aid in selecting a triggering mechanism, i.e. a means of detecting if a given frame has a laser pulse on it. Several triggering mechanisms are possible. Triggering on a certain peak pixel value is computationally simple, but raises the MED due to the solar background. Triggering on line width is more computationally intensive, but keeps the MED low.

The arc lamp was used as a solar simulator. With an OD 1.6 filter, it emitted 78 uW/cm^2 , which is approximately what the sun emits between 400 and 800 nm. On the CCD detector this gave a spectrum which peaked at 550 nm with $Z = 868$. This detector response was equivalent to that of an Nd:YLF pulse of 8.9 nJ/cm^2 , or $1/686$ MPE. Using the CID array, the arc lamp was not visible in the thermal noise.

Based on these results, there seems to be little benefit from using any triggering method more complex than peak count level for detecting MPE level laser pulses.

Saturation Behavior

Both the CID and CCD detectors were tested to see how they reacted to pulses above the saturation level. To test saturation behavior, peaks of various energy levels were used and the FWHM was measured in both the x and y directions. The results for both the CID and CCD are given in Figure 4.9. The CCD detector bloomed in the x direction, hence losing wavelength information. It took approximately 850 times the saturation level of an individual pixel to fill an entire row of the CCD. The blooming was roughly even on each side of the centroid, which would allow for some interpolation. No blooming was detected with the CID.

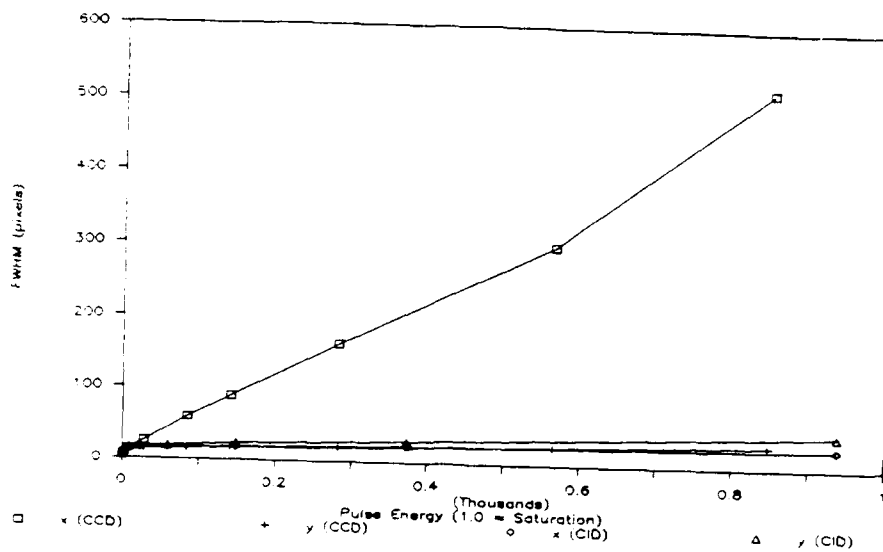


Figure 4.9. Saturation behavior.

V. Conclusion

This thesis presents the design, analysis, and test results of a device capable of detecting and characterizing laser radiation. The design was optimized to detect laser radiation intended to blind or daze aircrews and sensors. Its primary functions are to collect data on the threat laser and provide aircrew warning.

The system performed well in measuring wavelength and angle of arrival, but was not as accurate at measuring incident pulse energy. The system measured angle of arrival accurately within 1° at a single wavelength. The wavelength calibration was accurate to within 1 nm at a single angle of arrival. Measurements of pulse energy per unit area varied by $\pm 10\%$ for very small changes on angle of arrival. System responsivity had strong wavelength and angle of arrival dependencies.

The Minimum Laser Pulse Energy Detectable (MED) was thermal noise limited and hence varied strongly with detector temperature. Using the CCD detector at -10°C the MED was $.28 \text{ nJ/cm}^2$, or $1/23,000$ the Maximum Permissible Exposure (MPE) at a wavelength of 632 nm. The CID detector was operated at room temperature and had an MED of $.132 \text{ uJ/cm}^2$, or $1/45$ of the MPE for the same wavelength. Based on these figures, the need to cool the detector is

debatable.

The effects of solar radiation in the field of view had a negligible effect on system performance. When a solar simulator was used, the CCD detector gave the same peak value as it did when a laser pulse of 5.4 nJ/cm^2 , or 1/1100 of the MPE was incident. The solar simulator was not detectable above the thermal noise using the CID. Therefore, using a threshold value to determine if a laser pulse is in a frame of data should be adequate without resorting to line width measurement.

When irradiated above the saturation level, the CCD array bloomed horizontally, while the CID array did not bloom at all. The blooming of the CCD array grew slowly with pulse energy, filling one row of the detector when a pulse 850 times the saturation level was incident. Since the user can adjust the thruput using neutral density filters, blooming characteristics should not be an overriding factor in choosing a detector type.

It was found that the entrance optics were relatively insensitive to alignment. The only exception was defocus of the fiberbundle face. The spot size increased dramatically when the fiberbundle face was more than $\pm 1.5 \text{ mm}$ from the focal plane.

It is hoped that sufficient information has been presented in this thesis to permit a go/no-go decision be

made on contacting for a flyable model. The only item recommended for further research is an evaluation of the pixel size which will provide an optimum balance between wavelength and AOA resolution, and pulse energy accuracy. As was stated in the introduction, signal processing requirements for the system were not addressed.

Bibliography

1. Miyamoto, Kenro. "Fish Eye Lens," Journal of the Optical Society of America, 54: 1060-1061 (August 1964).
2. Lerner, J. M. and A. Thevenon. "The Optics of Spectroscopy, A Tutorial V2.0," New Jersrey: Instruments SA, Inc., 1988.
3. Smith, Warren J. "Modern Optical Engineering," New York: Mcraw Hill, 1966.

Vita

Captain Robert D. Kaiser [REDACTED]
[REDACTED]
[REDACTED]

[REDACTED] in 1981 [REDACTED] attended Rensselaer Polytechnic Institute, from which he received the degree of Bachelor of Science in Physics in May 1985. Upon graduation, he received a commission in the USAF through the ROTC program. For three years he was assigned to Aeronautical Systems Division at Wright-Patterson AFB as the Integrated Logistics Support Manager for the TR-1 Ground Station Program. He entered the School of Engineering, Air Force Institute of Technology, in June 1985.

UNCLASSIFIED

SECURITY CLASSIFICATION OF THIS PAGE

REPORT DOCUMENTATION PAGE

Form Approved
OMB No. 0704-0188

1a. REPORT SECURITY CLASSIFICATION UNCLASSIFIED			1b. RESTRICTIVE MARKINGS		
2a. SECURITY CLASSIFICATION AUTHORITY			3. DISTRIBUTION/AVAILABILITY OF REPORT Approved for public release; distribution unlimited		
2b. DECLASSIFICATION/DOWNGRADING SCHEDULE					
4. PERFORMING ORGANIZATION REPORT NUMBER(S) AFIT/GEP/ENP/89D-6			5. MONITORING ORGANIZATION REPORT NUMBER(S)		
6a. NAME OF PERFORMING ORGANIZATION School of Engineering		6b. OFFICE SYMBOL (If applicable) AFIT/ENP		7a. NAME OF MONITORING ORGANIZATION	
6c. ADDRESS (City, State, and ZIP Code)			7b. ADDRESS (City, State, and ZIP Code)		
8a. NAME OF FUNDING/SPONSORING ORGANIZATION		8b. OFFICE SYMBOL (If applicable)		9. PROCUREMENT INSTRUMENT IDENTIFICATION NUMBER	
8c. ADDRESS (City, State, and ZIP Code)			10. SOURCE OF FUNDING NUMBERS		
		PROGRAM ELEMENT NO.	PROJECT NO.	TASK NO.	WORK UNIT ACCESSION NO.
11. TITLE (Include Security Classification) ANALYSIS AND TEST OF A WIDE ANGLE SPECTROMETER (U)					
12. PERSONAL AUTHOR(S) Robert D. Kaiser Jr., B.S., Capt, USAF					
13a. TYPE OF REPORT MS Thesis		13b. TIME COVERED FROM _____ TO _____		14. DATE OF REPORT (Year, Month, Day) December 1989	
15. PAGE COUNT 93					
16. SUPPLEMENTARY NOTATION					
17. COSATI CODES			18. SUBJECT TERMS (Continue on reverse if necessary and identify by block number)		
FIELD	GROUP	SUB-GROUP			
20	05				
17	04	04	Laser Diagnostics, Optical Design, Spectrometer		
19. ABSTRACT (Continue on reverse if necessary and identify by block number)					
Title: ANALYSIS AND TEST OF A WIDE ANGLE SPECTROMETER					
Thesis Chairman: Dr. James Targove, Capt, USAF Assistant Professor of Engineering Physics					
20. DISTRIBUTION/AVAILABILITY OF ABSTRACT <input checked="" type="checkbox"/> UNCLASSIFIED/UNLIMITED <input type="checkbox"/> SAME AS RPT <input type="checkbox"/> DTIC USERS			21. ABSTRACT SECURITY CLASSIFICATION UNCLASSIFIED		
22a. NAME OF RESPONSIBLE INDIVIDUAL Capt James Targove			22b. TELEPHONE (Include Area Code) (513) 255-4498		22c. OFFICE SYMBOL AFIT/ENP

Abstract

A design for a device to measure wavelength, angle of arrival, and energy of a laser pulse is analyzed and tested. The instrument has a 180° field of view and an operating range of 400 nm - 800 nm. In a series of tests the instrument was found to measure angle of arrival accurately to within ± 41 arc minutes and a wavelength to within 1 nm. A variation of $\pm 20\%$ in the measurement of pulse energy per unit area was found for small changes in angle of arrival. The system was thermal noise limited and could detect a pulse that was $1/45$ of the Maximum Permissible Exposure (MPE) with an uncooled detector. When using a detector cooled to -10°C , the system could detect a pulse $1/22000$ of the MPE.